Implementing a sol-gel route to adjust the structural and dielectric characteristics of Bi and Fe co-doped BaTiO$_3$ ceramics

*Hamida Gouadria[1, *], Mourad Smari[2], Taoufik Mnasri[1], Jalloul Necib[1], Jesús López Sánchez[3,4],*

Pilar Marín[3], Atul P. Jamale[5], Rached Ben Younes[1]

[1]*Laboratory of Technology, Energy and Innovative Materials, TEMI, Department of Physics, Faculty of Sciences of Gafsa, University of Gafsa, 2112, Tunisia*

[2]*A.Chelkowski Institute of Physics, University of Silesia in Katowice, 75 Pulku Piechoty 1, 41-500, Chorzow, Poland.*

[3]*Instituto de Magnetismo Aplicado (IMA), UCM-ADIF, 28230 Las Rozas, Spain.*

[4]*Instituto de Cerámica y Vidrio (ICV-CSIC), 28049 Madrid, Spain*

[5]*CICECO-Aveiro Institute of Materials, Department of Materials and Ceramic, Engineering, University of Aveiro, 3810-193 Aveiro, Portugal.*

[*]*Corresponding author:*

Hamida Gouadria: hamidagouadria@gmail.com

Abstract:

The present work explores the impact of Fe insertion on the physical properties of Ba$_{0.95}$Bi$_{0.05}$Ti$_{1-x}$Fe$_x$O$_3$ (x=0.025, 0.050, and 0.075) prepared via sol gel method. The resulting samples crystallize in the tetragonal structure with space group *P4mm* and their morphological features point out the variation of the microstructure with Fe content. In turn, the dielectric constant versus temperature plot reveals the existence of two transition phases: the first one is ferroelectric-paraelectric transition phase (T$_{F-P}$) and the second one is ferroelectric orthorhombic - ferroelectric tetragonal phase (T$_{O-T}$). Analysis of conductivity curves using Jonscher's augmented equation (for x=0.025) and Jonscher's power law (for x=0.075) suggests the Non-Overlapping Small Polaron Tunneling (NSPT) model as a conduction mechanism.

***Keywords*:** *Dielectric properties, AC conductivity, NSPT model, Activation energy, VRH model.*

1. Introduction

Perovskite materials with general formula ABO_3 have attracted the attention of various researchers due to their interesting and versatile properties as ferroelectric, dielectric, magnetic, multiferroic, among others [1–4]. In this line, multiferroic materials are defined as materials in which more than one ferroic order (ferroelectric, ferromagnetic, and/or ferroelastic) coexist[5]. Currently, multiferroic materials draw the attention of researchers because of their wide applications such as spintronics, microelectronics, magnetic memory, and sensors[6]. A compound in which coexists both magnetic and electric polarization is rare in nature. $BiFeO_3$ (BFO) is probably one of the most studied multiferroic material by its nature with a rhombohedral distorted perovskite structure and space group R-3c at room temperature[4]. BFO is ferroelectric under T_C = 1103 K and antiferromagnetic below T_N = 643 K[7]. However, BFO possesses some drawbacks for room temperature operation devices such as high leakage current and large dielectric losses caused by oxygen vacancies[8]. As a result, BFO cannot be used in many applications due to the negatives points mentioned above. Aiming to extend the field of BFO's applications, some researchers have resorted to prepare a nanocomposite material by the combination of two or more materials. For example, (1-x) $(Al_{0.2}La_{0.8}TiO_3)$ +x $(BiFeO_3)$ nanocomposites display numerous interesting properties which could help to improve the use of BFO in many technological areas [9]. Specifically, the negative dielectric constant ε', negative dielectric loss ε'', and negatives electrical parameters for sample with x=0.4, demonstrate that these samples could be applicable in energy harvesting, space applications, efficient microwave absorbers, antenna design, among others [9,10].

Generally speaking, ferroelectricity is governed by a transition metal compound with empty d-shells (d^0), while ferromagnetism required a transition metal compound with a partially filled d (d^n). In fact, the scarcity of these materials is explained by the contradiction between the conventional mechanism necessary for ferroelectricity (FE) and ferromagnetism (FM), what is called the problem as "d^0 vs. d^n".

In the aim of producing multiferroic materials, Liu et al[11] proposed three methods: (1) Let polar and magnetic active ions occupying various Wyckoff positions, (2) prepare a double perovskite in which one is ferroelectric and the other one is magnetic, and (3) prepare a magnetic perovskite in which ferroelectricity is related to spiral magnetic order. Moreover, there were several approaches towards the investigation of a multiferroic materials, several investigations have resorted to doping in the site B of the ferroelectric materials with

transition metal atoms. In the family of perovskites oxides ABO_3, barium titanate $BaTiO_3$ (BTO) is an interesting compound because of its ferroelectric properties and its high dielectric constant. BTO is a ferroelectric prototype which goes through a sequential crystal structure transitions with temperature from ferroelectric to the paraelectric phase[2]. The ferroelectric effect observed in the tetragonal BTO is due to the displacement of Ti ions along the c-axis from its centro-symmetrical position in the unit cell, favoring the creation of an electric dipole. Despite its important ferroelectric and dielectric properties, BTO also presents some drawbacks like a high leakage current, relatively low Curie temperature, and a weak piezoelectric response. In order to improve its properties, BTO is usually doped or substituted by specific elements[12–15]. In the present study, we focus on Bi-substitutions in the BTO system since local structural distortions are effectively generated, providing new rotation polarization pathways [16,17]. Regarding its synthesis, several researchers prepare Bi-substituted $BaTiO_3$ ceramics via solid state reaction [18–20]. Nevertheless, some other researchers use the sol-gel method because of its low processing temperature, the obtained samples display a high purity and homogeneity, and it is achieved an excellent stoichiometry control of the products[21–23].

Interestingly, Tihtih et al[24] have investigated the effect of Bi on the structural and optical properties of $BaTiO_3$ nanoceramics via sol-gel method. They have found a decrease in the band gap which suggest that the prepared samples can be used in optoelectronic applications. Based on the findings of Islam et al[19], Bi-doped BTO could also minimize the dielectric losses and the AC electrical conductivity was found maximum for 5% of Bi doping BTO. In addition to the specific concentration of 5% of Bi doping, a maximum of the dielectric constant is achieved in other works[25]. Finally, according to Maurya et al[18], Bi doping into BTO could ameliorate ferroelectric properties as well, since Bi could promote an increase in both remanent polarization P_r and the coercive field E_c. Therefore, the addition of Bi can offer a wide range of improved ferroelectric properties with respect to the BTO ones using relatively lower percentages.

As mentioned in previous research, BTO with tetragonal structure is a ferroelectric material. Doping with a transition metal element in the Ti sites can provide magnetic features in BTO as well as improve its ferroelectric properties. Various works have investigated doped BTO with a transition metal (Cr, Mn, Fe, Co, Ni, and Cu) in the Ti sites [26–30]. Specifically, Fe-doped BTO was prepared by various methods like hydrothermal [26] , solid state [31] and sol-gel method[32]. Guo et al[33] showed that doping with Fe could lead to enhance both ferroelectric and magnetic properties. As identified by Khirade et al [34], doping with Fe

ameliorates dielectric properties of BTO since the conductivity increases as temperature rises, showing a semiconducting behavior in the compounds. Also, they noted that the dielectric properties were higher at low frequencies.

Recently, several researchers focused on doped-BTO in both sites A (Ba) and B (Ti), among which Bi and Fe stand out because of their unique multiferroic properties. In this line, Gouitaa et al [35] have studied the effect of Fe on the structural and dielectric properties of $Ba_{0.95}Bi_{0.05}Ti_{1-x}Fe_xO_3$ (x = 0, 0.1 and 0.2), using the solid-solid method. Yansen et al[36], have elaborated and reported the structural and multiferroic properties of $Ba_{0.95}Bi_{0.05}Ti_{1-x}Fe_xO_3$ ($0 \leq x \leq 0.1$) via solid-solid process. Electrical properties of $Ba_{0.92}Bi_{0.08}Ti_{0.92}Fe_{0.08}O_3$ have been reported by Wang et al [37]. These are examples of how new strategies are being pursued to try to confer noticeable improvements in ferroelectric properties while obtaining a magnetic response.

For those reasons, we have synthesized Bi and Fe co-doped BTO with different concentrations by the sol-gel method with the objective of examining the structural and dielectric properties of $Ba_{0.95}Bi_{0.05}Ti_{1-x}Fe_xO_3$ with x = 0.025, 0.050 and 0.075. The purpose of this research is to investigate the effects of temperature and frequency on the electrical and dielectric properties. In this regard, the electrical conductivity, dielectric constants, and electrical impedance as a function of the frequency and temperature are thoroughly examined.

2. Experimental procedure

3.1 Sol-gel synthesis

The $Ba_{0.95}Bi_{0.05}Ti_{1-x}Fe_xO_3$ with x = 0.025, 0.05 and 0.075, were prepared using sol-gel processes (see Fig.1). After weighing in stoichiometric proportions $Bi(NO_3)_2 \cdot 5H_2O$ (98%, Sigma-Aldrich), $Ba(NO_3)_2$ (99%, Sigma-Aldrich) and $Fe(NO_3)_3 \cdot 9H_2O$ (98%, Sigma-Aldrich), they were dissolved in distilled water for 1 hour at room temperature using a heating plate equipped with a magnetic stirrer. The temperature was then increased up to 60 °C and absolute ethanol (CH_3CH_2OH, 99.8% LabKem) plus titanium isopropoxide $Ti(OCH(CH_3)_2)_4$ (97%, Sigma-Aldrich) were added, followed by a few drops of the nitric acid HNO_3 (69%, Sigma-Aldrich). A homogenous viscous solution was obtained and it was subsequently dried at 85 °C for 24 hours. Afterwards, the resulting powder was milled and calcined at 750 °C for 12 hours in an air environment. Finally, the calcinated powder was milled again and sintered at 1000 °C for 2 hours in an air environment.

3.1 Characterization techniques

Phase composition and crystal structure was studied by X-ray diffraction (XRD) using a Cu-Kα radiation = 1.541874 Å). The range employed was from 20 to 85° with a step size of 0.03°. Morphological features and microstructure were determined by scanning electron microscopy (SEM), the morphologies of all samples $Ba_{0.95}Bi_{0.05}Ti_{1-x}Fe_xO_3$ were identified (SEM). Image processing was performed by the ImageJ software to estimate the particle size distribution. Optical properties were performed using Fourier Transform Infrared (FTIR) spectroscopy. Dielectric properties were examined by impedance spectroscopy with an equipment HP4284A LCR meter as a function of the frequency and temperature.

3. Results and discussion

3.1 Structural analysis

The XRD of the samples shown in Fig.2 were analyzed using FullProf program[38]. The XRD patterns of $Ba_{0.95}Bi_{0.05}Ti_{1-x}Fe_xO_3$ ceramics with x=0.025, 0.05, and 0.075 are found to match the tetragonal phase with space group P4mm. The lattice parameters calculated from the FullProf fit are given in Tab.1. There is a good agreement between the observed and calculated profile since the values of $\chi^2 < 1.93$.

Fig.3 shows a slight shift of the diffraction peak (111) towards lower angles with the increase in Fe concentration. The splitting in the peaks (200) and (002) around $2\theta = 45°$ can be detected for all the samples (Fig.4). These two peaks appear to merge into each other when the Fe doping is increased up to x=0.075 and it may be due a decrease in tetragonality (c/a) [36] (see Tab.1). Islam et al [39] suggest that the loss of tetragonality is usually related to the stabilization of a cubic phase. However, the broadening of the peak (200) for x=0.075 is relatively wide, so it can be considered to be a pseudo-cubic structure and/or size effects. Tab.1 shows an increase of the lattice constant a, while there is a decrease in the lattice constant c. Therefore, the tetragonality ratio is reduced. Masó et al [40] also reported that the decrease in tetragonality is favored by increasing the Fe concentration. In addition, the cell volume of our samples rises with Fe doping (ionic radius 0.645 Å), which is probably due to the substitution of Ti^{4+} with ionic radius (0.605Å) (Tab.1) [41]. Similar results were obtained by Craciun et al [42]. Furthermore, the increase of the cell volume is generally related to a decrease in the strain [43]. For x=0.025, the sample shows a high purity since there no secondary phases are detected (Fig.2). Nevertheless, x=0.05 and 0.075, an unknown secondary phase (called as X in Figure 2) appears with a relatively low percentage of 2.96% and 0.52%, respectively. Therefore, the X-phase disappears by increasing the Fe content. Subsequently, an estimation of the crystallite size is calculated for several methods:

i. Scherrer method

The general method to determine crystallite size is by Debye Scherrer equation[44]:

$$D = \frac{K * \lambda}{\beta \cos \theta} \qquad (1)$$

Where D is the crystallite size (nm), λ is the wavelength, β is the full width at half maximum (FWHM) of the peak, θ is the diffraction angle of the peak, and K is a constant equal to 0.94 (considering particles with a spherical shape).

ii. Modified Scherrer method (MS)

In order to decrease the error in calculating crystallite size, the modified Scherrer equation is based on this principle through which the average crystallite size D is obtained via all major peaks by least square method [45]. Subsequently, the Scherrer modified formula can be written as:

$$\ln \beta = \ln \left(\frac{K * \lambda}{D} \right) + \ln \left(\frac{1}{\cos \theta} \right) \qquad (2)$$

By plotting $\ln \left(\frac{1}{\cos \theta} \right)$ as a function of a graph between $ln\beta$, a linear fit is obtained (see Fig.5) with an intercept value equal to $y_{intercept} = ln \left(\frac{K * \lambda}{D} \right)$.

$$D = \frac{K * \lambda}{Exp^{y_{intercept}}} \qquad (3)$$

iii. Williamson –Hall plot method (W-H)

Scherrer formula considers only the impact of crystallite size on the XRD peak broadening. However, the lattice strain of the material could also causes a broadening of the diffraction peaks[43,46].

The total broadening can be written as:

$$\beta_{Total} = \beta_D + \beta_S \qquad (4)$$

From equation (1) we can write broadening of crystallite size [46]:

$$\beta_D = \frac{K * \lambda}{D \cos \theta} \qquad (5)$$

$$\beta_S = 4 * \varepsilon \tan \theta \qquad (6)$$

$$\beta_T = \frac{K * \lambda}{D \cos \theta} + 4 * \varepsilon \frac{\sin \theta}{\cos \theta} \qquad (7)$$

Finally, we get: $\qquad \cos\theta * \beta_T = 4 * \varepsilon * \sin\theta + \frac{K*\lambda}{D}$ (8)

After plotting, $\cos\theta * \beta_T$ versus $4 * \sin\theta$ should be a straight line where the slope provides the strain ε and the $y_{intercept}$ gives the value of $\frac{K*\lambda}{D}$ (see Fig.6).

iv. Size strain plot method

W-H plot shows that the broadening is essentially isotropic which means that diffracting domains are also isotropic and there is also a contribution of micro strain. Size strain plot (SSP) is a method which considers that the XRD peak profile is a combination between Lorentzian and Gaussian function, where the crystallite size broadened profile comes from the Lorentzian function (β_L) and the strain broadened profile comes from the Gaussian function (β_G) [47]. The total broadening of SSP can be expressed as:

$$\beta_T = \beta_L + \beta_G \qquad (9)$$

Besides, the SSP method gives always a better result for an isotropic broadening as it provides an importance for lower angles reflections since accuracy is more than at higher angles. The SSP method is performed using the following equation[47,48]:

$$(d_{hkl} * \beta_{hkl} * \cos\theta)^2 = \frac{K*\lambda}{D} * (d_{hkl}^2 * \beta_{hkl} * \cos\theta) + \frac{\varepsilon^2}{4} \qquad (10)$$

Where d_{hkl} is the lattice distance between the (h k l) planes. Similarly, to W-H plot, we plot $(d_{hkl} * \beta_{hkl} * \cos\theta)^2$ versus $(d_{hkl}^2 * \beta_{hkl} * \cos\theta)$, obtaining the crystallite size from the slope and the strain from the $y_{intercept}$ (see Fig.7).

The results obtained from Debye Scherrer, modified Scherrer, Williamson Hall plot, and SSP method are given in Tab.2. It can be noticed that the values obtained by the different models vary systematically. Specifically, it is evidenced from Tab.2 that the modified Scherrer method is close to the result obtained by the Debye Scherrer one. However, SSP method shows a large variation related to the difference in the average of the crystallite size distribution since it can be modified by the inclusion of strain. In this regard, it is considered from Tab.2 that there is an inversely relationship between crystallite size and strain[43,49] and similar results have been observed in some doped $BaTiO_3$ samples[50–52]. The obtained nano-metric size is probably due to the method of preparation used in this work.

3.2 Morphological analysis

A morphological characterization is carried out by SEM in order to obtain an accurate estimation of the microstructure and morphology of the samples. SEM images of $Ba_{0.95}Bi_{0.05}Ti_{1-x}Fe_xO_3$ ceramics illustrated in the inset of Fig.8 show that the microstructure

exhibits a variation with Fe content. The observed distribution can be described using a Lorentz fit (Fig.8/ (a, b, and c)). The average grain size was calculated from SEM images using the ImageJ software and is depicted in Tab.3. As can be observed, the grain size decreases as Fe content increases. Similar results have been reported in some dopants within the BTO system[53,54].This decrease may be explained in terms of the formation of grains with lower sizes with the increase of Fe content. It is clear that the average grain size is larger than crystallite size, indicating that each grain size observed by SEM consists of numerous nanoparticle domains.

3.3 FTIR analysis

The FT-IR transmission spectra of the $Ba_{0.95}Bi_{0.05}Ti_{1-x}Fe_xO_3$, in the range of 400-1500 cm^{-1} at room temperature is represented in Fig.9. The absorption bands from 400 to 858 cm^{-1} are attributed to the stretching vibrations of Ti-O band which are characteristic for BTO [55–59]. Besides, bands located between 1100 – 1200 cm^{-1} are assigned to O-O stretching frequency[60]. As mentioned in the literature, bands between 1000 -1700 cm^{-1} are assigned to organic groups[61]. Bands at around 1380 cm^{-1} are related to the deformation vibrations of CH_3. However, the modes ranging from 1400 to 1600 cm^{-1} are assigned to O-H bending vibrations[62], which may be a moisture coming from water in the KBr matrix[63,64]. Moreover, there are no additional contributions coming from the dopant. In this sense, there is only a shift in the Ti-O band accompanied by an improvement with the increase of Fe content (see Tab.4.), which it may confirm the effective incorporation of Fe^{3+} into Ti^{4+} sites[65,66].

3.4 Dielectric properties

3.4.1 Dielectric properties versus temperature

Dielectric measurements are taken at four distinct frequencies from room temperature to 660 °C (1 KHz, 10 KHz, 100 KHz, and 1 MHz). Fig.10/a shows the evolution of the dielectric constant ε as a function of temperature at 1 KHz for all samples. It is observed different maxima located at different temperatures depending on the Fe content. In order to describe correctly the evolution of the dielectric constant ε', we establish two different regions: the first one (R1) corresponds to a ferroelectric-paraelectric transition phase (T_{F-P}) located at the lower temperature region from 49 to 250 °C. The second one (R2) is related to the higher temperature region between 250 and 650 °C, in which a dielectric anomaly is observed for all samples. Starting for x=0.025, Fig.10/b represents the evolution of dielectric

constant at different frequencies. At the R1, it is noticed that ε'increases with temperature reaching a maximum at ~100 ºC, corresponding to the Curie temperature. The increase of ε'up to T_C is explained in terms of ferroelectric domains separation into numerous polar nano-regions. On the contrary, a decrease of ε'is detected after T_C and it is attributed to the phase transition from a ferroelectric to paraelectric state. However, in R2, ε'rises with temperature until reaching a new maximum value again which corresponds to a dielectric anomaly at the vicinity of 500 °C. This dielectric anomaly is relatively high and strongly dependent on the frequency since it decreases as frequency rises. Subsequently, the variation of dielectric constant for x=0.05 is shown in Fig.10/c. As observed, ε'also increases as temperature increases, irrespective of the studied frequencies. Similarly, ε'goes up slowly until 200 °C, then it increases rapidly towards the higher temperatures. Therefore, no peak is identified in the region R1. This behavior may be due linked to the evolution of the prepared sample in the paraelectric phase as mentioned by other researchers[67,68]. The dielectric anomaly is weakened and almost suppressed as frequency increases. The behavior could be attributed to Maxwell-Wagner mechanism of polarization where the grain boundary contribution is dominant. Similar results are proved by Gupta et al[69]. Likewise, Fig.10/d displays the variation of dielectric constant for x=0.075. ε' also rises with temperature and broadened maxima are shown in both regions (R1 and R2). Enlarged loops are illustrated especially for this sample from room temperature to 300°C (see Fig.11/a, b, c and d). All curves, except the first one at 1 KHz, display one peak in the region R1, suggesting a transition from the ferroelectric to the paraelectric phase. Regarding the region R2, all samples present one dielectric anomaly around 500 °C which decreases as frequency increases. This anomaly may correspond to the phase transition from ferroelectric-orthorhombic to the ferroelectric-tetragonal phase T_{O-T}, as mentioned by numerous works[35,70,71]. Interestingly, ε'possesses higher values at low frequencies, suggesting the presence of all types of polarization in the prepared compounds. Besides, the atomic number of Fe (Z_{Fe}=26) is higher than the atomic number of Ti (Z_{Ti}=22), which becomes the ionic polarization more important at low frequencies[72]. At higher frequencies, some of these types of polarizations could have a less contribution to the dielectric constant, leading to a dielectric dispersion behavior. In addition, the shift of the maxima to higher temperatures as frequency increases, indicates a relaxor behavior in our samples. As seen from Fig.10/a, dielectric constant, for x=0.05 is lower than for x=0.075. This reduction may be due to the formation of impurity phases in the ceramics[73], which is confirmed by the presence of a secondary phase (X-phase) in our samples as a residual contribution (2.96% for x = 0.05 and

0.52% for x = 0.075). Consequently, this secondary phase may cause the broadness of the dielectric constant, promoting a heterogeneous composition with various local dielectric constant values[73]. As a result, the rest of this study is focused on the dielectric properties for x=0.025 and x=0.075.

3.4.2 Dielectric properties versus frequency

3.4.2.1 Impedance analysis

The purpose of this section is the determination of the effect of Fe on $Ba_{0.95}Bi_{0.05}TiO_3$ ceramics by the impedance analysis, discerning between grain and grain boundary effects. The complex impedance Z^* can be written as:

$$Z^* = Z^{'}(\omega) - jZ^{''}(\omega) \qquad (11)$$

Where ω is the angular frequency ($\omega = 2\pi f$), and Z', Z'' are the real and imaginary parts of complex impedance, respectively.

Fig.12 / (a, b) represents the variation of Z' against frequency recorded at high temperatures (450-650 K) for both prepared samples. As shown, Z' presents higher values at a low frequency around $\sim 10^2$ Hz for x =0.025 and at a higher frequency, $\sim 10^4$ Hz for x=0.075, then it reduces with frequency. The high values of Z' at low frequencies and their decrease at higher frequencies could be attributed to the phenomenon of space charges accumulation at the interface[74]. By contrast, Z' declines as temperature rises, indicating a negative temperature coefficient of resistance NTCR behavior in our samples. Furthermore, the reduction of Z' with frequency and temperature, reveals an enhancement inversely proportional of the AC conductivity[75]. For x=0.025, the real part Z' above 10^5 Hz becomes frequency independent and the values merge for all the temperatures, manifesting the presence of a space charge polarization.

Fig.13 / (a, b) displays the frequency dependence on the imaginary part Z'' with temperature in range 450-650 K for both studied compounds (x=0.025 and 0.075). As seen in Fig.13, Z'' attaints a maximum value Z''_{max} for all the temperatures. A reduction in the magnitude of Z'' could be related to a reduction of the resistivity of the presented samples. Moreover, the Z'' curves possess a broad peak which moves to higher values of frequencies as temperature increases, suggesting the presence of relaxation phenomenon in our materials. This behavior use to be a result of the impact of the presence of defects and/or gaps for high temperatures and immobile species for low temperatures[76]. Additionally, the intensity of

the peak reduces with temperature accompanied by a large broadening for both studied samples, indicating that the conduction process are thermally activated in our compounds.

With the purpose of the separation between grain and grain boundary contributions to the electrical properties of $Ba_{0.95}Bi_{0.05}Ti_{0.975}Fe_{0.025}O_3$ and $Ba_{0.95}Bi_{0.05}Ti_{0.925}Fe_{0.075}O_3$ ceramics, the Nyquist plots are depicted in Fig.14/ (a, b). As observed, for the x=0.025 sample, it is detected an incomplete semicircle arc in the range 450-550 K and a semicircle in the range 575-650 K. For x=0.075, all the curves are characterized by the appearance of an incomplete semicircle. A decrease in the radius and the maximum of the experimental semicircles with the augmentation of temperature is displayed, suggesting a negative temperature coefficient of resistance NTCR behavior and also a semiconducting behavior in the studied samples. Moreover, the observed single semicircles and semi-arcs suggest that the grains are responsible for the conduction process[77]. Furthermore, the decentralization of the semicircles in the prepared samples also suggests a non-Debye type relaxation process. Besides, the reduction of broad nature of semicircles and arc of semicircles with temperature for both samples may be explained by the shift of the relaxation to high frequencies[74].

The impedance experimental data is fitted to extract the grain and grain boundary effects in our compounds, using Zview software to an equivalent circuit composed by series of two parallel combinations for both samples:

➢ For x=0.025, two regions appear: the first one between (RI) from 450 to 550 K and the second one (RII) from 575 to 650 K.

⊕ RI: grain resistance R_g, capacitance C_g and modified capacitance CPE_g (R_g // C_g // CPE_g), representing the contribution of grain, followed by the grain boundary contribution (R_{gb} // C_{gb} // CPE_{gb})

⊕ RII: grain resistance R_g and modified capacitance CPE_g (R_g // CPE_g), representing the grain contribution, followed by the grain boundary contribution (R_{gb} // CPE_{gb}).

➢ For x=0.075, the fitting process leads to a series combination of grain resistance R_g and capacitance CPE_g (R_g//CPE_g), showing the grain contribution followed by the grain boundary (R_{gb} // CPE_{gb}).

The theoretical parameters extracted from the fit of the experimental impedance are summarized in Tab.5. and. 6. Importantly, the resistivity of grain and grain boundary decrease as temperature increases, demonstrating the presence of a negative temperature

coefficient of resistance NTCR behavior in our samples. In turn, these features also indicate that both grain and grain boundary components ameliorate the conductivity. On the other hand, the decrease of the resistivity with temperature evidences a rise of the DC conductivity[78]. It is apparent that R_{gb} resistance is higher than R_g resistance. This results proves that grain conductivity is higher than the grain boundary grain one which is caused by the presence of voids between grain and the non-stoichiometric distribution of oxygen vacancy at the grain boundary[79].

Additionally, the overlapping of the grain at higher frequencies and the grain boundary at low frequencies are the mainly causes of the broadening peaks of the imaginary part Z'' with temperature.

For the determination of the conduction mechanism, a study of the electrical conductivity in our samples appears essentially. The electrical conductivity σ_g, σ_{bg}, and σ_{tot} are calculated using the previous values of grain resistance R_g and boundary grain resistance $R_{gb,}$ using the following equations:

$$\sigma_g = \frac{e}{R_g * S} \qquad (12)$$

$$\sigma_{bg} = \frac{e}{R_{gb} * S} \qquad (13)$$

$$\sigma_{tot} = \frac{e}{(R_g + R_{gb}) * S} \qquad (14)$$

The logarithmic variation of σ_g, σ_{gb} and σ_{tot} as a function of 1000/T is shown in Fig.15. The value of activation energy of the grain is greater than the grain boundary one, indicating a higher electrical conductivity of the grain behavior. As seen in Tab.7, the activation energy is found to decrease by increasing the doping ratio. This decrease could be related to the greater conductivity of grain and grain boundary for x=0.075. According to Chchiyai et al[80], a lower activation energy is associated with a higher conductivity.

To investigate the intrinsic response of the prepared samples and the dependence of the real part Z' on temperature, we calculate the average normalized change (ANC) via the following equation:

$$ANC = \frac{\Delta Z'/\Delta f}{Z'_0} \qquad (15)$$

Here, $\Delta Z' = \Delta Z'_{low} - \Delta Z'_{high}$, $\Delta f = \Delta f_{high} - \Delta f_{low}$, where Z'_{low} and Z'_{high} are the corresponding values of Z' respectively at low and high frequencies, noted f_{low} and f_{high}. $Z'(0)$ is the value of Z' at zero frequency for all temperatures[81].

The evolution of ANC vs. temperature for the studied samples is illustrated in Fig.16/a. For x=0.025, ANC starts to decline slowly in the range of 450-550 K and it continues to decreases rapidly. For x=0.075, ANC decreases rapidly as temperature increases. These behaviors describe not only the decrease of the trapped charge carriers density, but also, the existence of various conduction processes[82]. A representation of $d(ANC)/d(T)$ is depicted in Fig.16/b. For x=0.075, a modification of the slope occurred at a specified temperature called temperature of average normalized change T_{ANC}. In these temperatures, all the trapping centers become empty. Two different temperatures are detected $T_{ANC1} = 550$ K and $T_{ANC2} = 600$ K. The first one at $T_{ANC1} = 550$ K, it is suggested a change in the conduction mechanism, whereas at the second one at $T_{ANC2} = 600$ K, the total disappearing of the trapping charges leads to the activation of other conduction mechanism[83]. By contrast, the trapping centers are not be empty for x=0.025 and some charge carriers are still frozen. This means that the x=0.025 sample requires a higher temperature to release all the trapping centers[84].

3.4.2.2   Electrical study
3.4.2.2.1   AC conductivity regime

Fig.17// (a, b) shows the variation of electrical conductivity of $Ba_{0.95}Bi_{0.05}Ti_{0.975}Fe_{0.025}O_3$ and $Ba_{0.95}Bi_{0.05}Ti_{0.925}Fe_{0.075}O_3$, in the range 450-650 K for frequencies varying from 10 Hz to 1 MHz Two different regions can be discerned in the curves. At the low frequency region, the conductivity is stable, indicating a non-dependence frequency nature for conductivity, evidencing the DC conductivity (σ_{DC}). However, the conductivity rises at high frequencies and represents a dispersion behavior. The obtained high values of AC conductivity at high frequencies is explained by the oscillation of electric dipoles with high velocity[77]. At low frequencies, DC conductivity increases by increasing the temperature due to the long-distance movement of the charge carriers. The increase of σ_{AC} with temperature, suggests the presence of a semi-conductor behavior in our materials.

To determine the conduction mechanisms, we focus on the variation of AC conductivity σ_{AC} which follows the Jonscher's universal power law[85]:

$$\sigma_{AC} = \sigma_{DC} + A\omega^s \quad (16)$$

where σ_{DC} represents the DC conductivity, A is a temperature dependent constant which is the dispersion factor representing the strength of polarizability, and s is an exponent function of temperature which refers to the degree of interaction between the lattice and the mobile carrier.

For x=0.075, the total conductivity is adjusted using the equation (16). A good agreement between the experimental data and fit is observed (see Fig.17// (c, d)), which means that this sample obeys to the Jonscher's universal power law. On the contrary, this law cannot be applied to the other sample.

For x=0.025, the total conductivity is adjusted using the following equation:

$$\sigma_{AC}(\omega) = \frac{\sigma_s}{1 + \tau^2\omega^2} + \frac{\sigma_\infty\tau^2\omega^2}{1 + \tau^2\omega^2} + A\omega^S \qquad (17)$$

where σ_s is the conductivity at low frequencies, σ_∞ is an estimate of conductivity at high frequencies, τ represents the characteristic relaxation time, ω is the angular frequency. The detailed analysis of the total conductivity is perfectly adjusted using the equation (17), showing a good confirmation between theoretical fit and experimental data (see Fig.17// (c, d)).

A plot of the s-T variation is necessary for the determination of the conduction mechanism. The variation of s with the temperature dependence is described by numerous theoretical models. Fig.18// (a, b) depicts the s-T variation of the two samples with x= 0.025 and 0.075. s increases with temperature, suggesting the non-overlapping small polaron tunneling (NSPT) model for the two specimens. In this case, the exponent s can be written as[86]:

$$s = 1 + \frac{1 + 4K_BT}{W_M - K_BTln(\omega\tau_0)} \qquad (18)$$

where W_M is the maximum barrier height, representing the polaron hopping energy, τ_0 is the characteristic relaxation time, ω is the angular frequency and K_B is the Boltzmann constant. In the case of large values of W, equation (18) can be approximated to:

$$s = 1 + \frac{1 + 4K_BT}{W_M} \qquad (19)$$

W_M is calculated from the slope of the curve 1-s against T, as represented in Fig.18// (c, d). The calculated values are 0.178 and 0.238 eV for x=0.025 and 0.075, respectively.

3.4.2.2.2   DC conductivity regime

At lower temperatures, the DC conductivity could be described using a variable range hopping VRH model described by Mott law's equation:

$$\sigma_{DC} = \sigma_0 e^{(-T_0/T)^{1/4}} \qquad (20)$$

with σ_0 is a constant and T_0 is Mott's characteristic temperature.

Using this model, the hopping range can be larger than the distance between the neighboring equivalent sites, which is caused by the small activation energy by the VRH model[87]. The logarithmic variation of DC conductivity as a function of $T^{-0.25}$ at 1 KHz, 10 KHz, and 100 KHz, for both samples is illustrated in Fig.19/ (a, b). The linear variation of the plotted curves proves the hypothesis given by Mott[87]. The decrease in the concentration of the free carriers at low temperatures and the present low thermal energy (no hopping process activation), are responsible for the generated behavior. Similar results are obtained by others researchers[88,89]. The extracted values of T_0 are indicated in Tab.8.

The characteristic temperature T_0 is equal to:

$$T_0 = \frac{16}{K_B N(E_F)\alpha^3} \qquad (21)$$

where K_B is the Boltzmann's constant, N (E_F) represents the density of states in the area of the Fermi level, and α is the localized length (~2.22 nm).

As seen in Tab.8, N(E_F) increases with Fe content, which is in a good agreement with the variation of the grain activation energy.

The hopping energy W can be calculated using the following equation:

$$W = \frac{K_B T^{3/4} T_0^{1/4}}{4} \qquad (22)$$

The thermal variation of hopping energy W(T) (see Fig.20/ (a, b)) shows an increase with temperature, suggesting a polaronic VRH conduction dynamic for both samples.

In the same figure, the meaning hopping distance R_h is calculated via the below equation:

$$R_h = \frac{3}{8}\alpha(\frac{T_0}{T})^{1/4} \qquad (23)$$

It is clear from the thermal variation of R_h (T) (see Fig.21/ (a, b)), that hopping distance decreases with temperature until reaching a maximum temperature of 550 K for x=0.025 (RI) and 650 K for x=0.075 (RII). The results correspond to the shortest hopping distance and promote the robustness of the VRH model. In turn, those temperatures are associated with the crossover point from VRH model to Arrhenius model[89].

The variation of DC conductivity is proportional to temperature (see Fig.22/ (a, b)), indicating the presence of a semiconductor behavior in our materials. In particular, the variation of the conductivity obeys to SPH model, defined by the following relation[90]:

$$\sigma_{DC} * T = A e^{\frac{-Ea}{K_B T}} \qquad (24)$$

where A is a constant, Ea is the activation energy, K_B is Boltzmann's constant and T is the absolute temperature.

The logarithmic variation of DC conductivity (σ_{DC} *T) as a function of 1000/T is represented in Fig.22/(c, d) for 1 KHz, 10 KHz, and 100 KHz. They feature a linear variation, indicating the activation of the small polaron hopping (SPH) process[89]. The calculated values of Ea are calculated from the slope of the curves and they are summarized in Tab.9. The activation energy is inversely proportional with frequency. This decrease proves that the applied frequency could enhance the jumps of charge carriers between localized states[91]. Additionally, the increase of the AC conductivity with frequency are attributed to small values of activation energy, suggesting that the conduction mechanism could be expressed using Tunneling conductivity[91].

3.4.2.3   Dielectric permittivity versus frequency:

A study of the dielectric permittivity is carried out to obtain more information about the relaxation phenomenon. The variation of the real part of the permittivity $\varepsilon^{'}$ and the dielectric loss $\varepsilon^{''}$ are shown in Fig.23/ (a, b, c, and d). It is evidenced that, for both samples, ε'and ε''are dependent of temperature at low frequencies. However, all curves merge into each other at high frequencies, displaying a constant trend. This particular behavior was attributed to Koop's phenomenon or also called "double layer dielectric model", which illustrates that larger values of ε'and ε''could be achieved at lower frequencies[92]. Following this model, the polycrystalline perovskite is formed by two layers, one for the core of the grains (higher conductivity) and the other for the boundary of the grains (lower conductivity). In this sense, the grain boundaries are more active at low frequencies[77], implying that the charge carriers are piled up at the grain boundary interface when a polarization is applied. The energy of the charge carriers is lower compared to the energy of the grain boundaries and a condition of saturation polarization is reached in this frequency range. As a result, they act like additional electrical dipoles leading to an improvement of the charge polarization distribution. However, the electrical dipoles do not follow the applied field when high frequencies are applied. The charge carriers absorb the energy and some charges break the grain boundary interface,

reaching a situation of electric grain conduction. In this regime, a decrease of the ε' and ε'' is noticed, promoting a rise of the AC conductivity as frequency increases[93–95].

As mentioned in the literature, the higher value of ε'at low frequencies suggests the presence of all types of polarizations (interfacial, dipolar, electronic, and ionic). Specifically, to low frequencies, dipolar and interfacial polarizations are dominant and they are strongly dependent on temperature. On the contrary, electronic and ionic polarizations are dominant at high frequencies[84]. In addition, ε'decreases as frequency increases. According to Panday et al[96], this decrease of ε'could be related to the presence of space charge polarization and the polaron contribution. Furthermore, the high value of polarization and the charges mobility are responsible of the augmentation of the ε' [97].Finally, ε''increases as temperature increases, suggesting the dependence of relaxation time on temperature. The greater values of dielectric constant are linked with a low dielectric loss, promoting that both samples can be suitable for dielectric materials.

4. Conclusion

The sol-gel method is used to fabricate series of $Ba_{0.95}Bi_{0.05}Ti_{1-x}Fe_xO_3$ (x = 0.025, 0.05, and 0.075). All samples exhibit a tetragonal phase and a pseudo-cubic phase (P4mm) occurs as doping concentration increases. With increasing x, cell volume increases, while tetragonality decreases. The size of crystallites is determined using several methods, including Debye Scherrer, modified Scherrer, W-H plot, and size strain plot. When compared to other models, the modified Scherrer approach is more accurate than the Debye Scherrer one. SEM data show that the grain size is approximately 1.967, 1.711, and 0.402 μm (for x = 0.025, 0.05, and 0.075, respectively). The dielectric constant with temperature reveals the presence of two-phase transitions (T_{F-P} and T_{O-T}). The contribution of grain and grain boundaries influence on the electrical properties of the samples is confirmed by impedance measurements. The presence of a thermally activated relaxation process is revealed by the complicated impedance analysis. For x=0.025, the conductivity spectra are well fitted by the enhanced Jonscher's equation, and for x=0.075, the Jonscher's power law. The non-overlapping small polaron NSPT model is used to calculate conductivity for both samples. The DC conductivity proves a VRH process at low temperatures and a SPH model at high temperatures. The dielectric constant vs frequency exhibits huge values at lower frequencies, implying that both dipolar and interfacial polarizations are present. Consequently, the compounds under study possess various properties such as NTCR behavior, a high dielectric

constant, and moderate dielectric losses. These trends make these compositions suitable for thermal sensor, energy, and/or high-frequency applications.

Declaration of interests

☒ *The authors declare that they have no known competing financial interests or personal relationships that could have appeared to influence the work reported in this paper.*

☐ *The authors declare the following financial interests/personal relationships which may be considered as potential competing interests.*

References:

[1] C. Henchiri, R. Hamdi, T. Mnasri, M.A. Valente, P.R. Prezas, E. Dhahri, Structural and magnetic properties of La1-x☐xMnO3 (x = 0.1; 0.2 and 0.3) manganites, Appl. Phys. A. 125 (2019) 725. https://doi.org/10.1007/s00339-019-2980-3.

[2] C.W. Huang, L. Chen, J. Wang, Q. He, S.Y. Yang, Y.H. Chu, R. Ramesh, Phenomenological analysis of domain width in rhombohedral ${\text{BiFeO}}_{3}$ films, Phys. Rev. B. 80 (2009) 140101. https://doi.org/10.1103/PhysRevB.80.140101.

[3] L. Zhou, P.M. Vilarinho, J.L. Baptista, Dependence of the Structural and Dielectric Properties of Ba1-xSrxTiO3 Ceramic Solid Solutions on Raw Material Processing, J. Eur. Ceram. Soc. 19 (1999) 2015–2020. https://doi.org/10.1016/S0955-2219(99)00010-2.

[4] H. Felhi, R. Dhahri, M. Smari, E. Dhahri, E.K. Hlil, Magnetocaloric effect and critical behaviour of La0.5Ca0.2Ag0.3MnO3 compound, Chem. Phys. Lett. 733 (2019) 136632. https://doi.org/10.1016/j.cplett.2019.136632.

[5] T. Kimura, T. Goto, H. Shintani, K. Ishizaka, T. Arima, Y. Tokura, Magnetic control of ferroelectric polarization, Nature. 426 (2003) 55–58. https://doi.org/10.1038/nature02018.

[6] P. Rodgers, Nanoscience And Technology: A Collection Of Reviews From Nature Journals, World Scientific, 2009.

[7] J. Wang, J.B. Neaton, H. Zheng, V. Nagarajan, S.B. Ogale, B. Liu, D. Viehland, V. Vaithyanathan, D.G. Schlom, U.V. Waghmare, N.A. Spaldin, K.M. Rabe, M. Wuttig, R. Ramesh, Epitaxial BiFeO 3 Multiferroic Thin Film Heterostructures, Science. 299 (2003) 1719–1722. https://doi.org/10.1126/science.1080615.

[8] C. Ederer, N.A. Spaldin, Weak ferromagnetism and magnetoelectric coupling in bismuth ferrite, Phys. Rev. B. 71 (2005) 060401. https://doi.org/10.1103/PhysRevB.71.060401.

[9] A. Mallikarjuna, S. Ramesh, N.S. Kumar, K.C.B. Naidu, K.V. Ratnam, H. Manjunatha, Photocatalytic Activity, Negative AC-Electrical Conductivity, Dielectric Modulus, and Impedance Properties in 0.6 (Al0.2La0.8TiO3) + 0.4 (BiFeO3) Nanocomposite, Cryst. Res. Technol. 55 (2020) 2000068. https://doi.org/10.1002/crat.202000068.

[10] A. Mallikarjuna, S. Ramesh, N.S. Kumar, K.C. Babu Naidu, K.V. Ratnam, H. Manjunatha, B.P. Rao, Structural transformation and high negative dielectric constant

behavior in (1-x) (Al0·2La0·8TiO3) + (x) (BiFeO3) (x = 0.2–0.8) nanocomposites, Phys. E Low-Dimens. Syst. Nanostructures. 122 (2020) 114204. https://doi.org/10.1016/j.physe.2020.114204.

[11]   A brief review on perovskite multiferroics: Ferroelectrics: Vol 507, No 1, (n.d.). https://www.tandfonline.com/doi/abs/10.1080/00150193.2017.1283171   (accessed November 3, 2022).

[12]   G.H. Haertling, Ferroelectric Ceramics: History and Technology, J. Am. Ceram. Soc. 82 (1999) 797–818. https://doi.org/10.1111/j.1151-2916.1999.tb01840.x.

[13]   E. Yeceu, H. Laysandra, D. Triyono, Effect of Sr substitution on electrical polarization of Ba1-xSrxTiO3 (x = 0.0, 0.2, 0.6, and 0.8) perovskite materials, J. Phys. Conf. Ser. 1442 (2020) 012020. https://doi.org/10.1088/1742-6596/1442/1/012020.

[14]   H.A. Gatea, I.S. Naji, Effect of Grain Size and Sintering Temperature on Dielectric Properties of Perovskite Ba0.5Sr0.5TiO3, (2018) 9.

[15]   M.V. Zdorovets, A.L. Kozlovskiy, Study of the effect of La3+ doping on the properties of ceramics based on BaTiOx, Vacuum. 168 (2019) 108838. https://doi.org/10.1016/j.vacuum.2019.108838.

[16]   D.S. Keeble, E.R. Barney, D.A. Keen, M.G. Tucker, J. Kreisel, P.A. Thomas, Bifurcated Polarization Rotation in Bismuth-Based Piezoelectrics, Adv. Funct. Mater. 23 (2013) 185–190. https://doi.org/10.1002/adfm.201201564.

[17]   R. Seshadri, N.A. Hill, Visualizing the Role of Bi 6s "Lone Pairs" in the Off-Center Distortion in Ferromagnetic BiMnO $_3$, Chem. Mater. 13 (2001) 2892–2899. https://doi.org/10.1021/cm010090m.

[18]   D. Maurya, S. Priya, Effect of Bismuth Doping on the Dielectric and Piezoelectric Properties of Ba $_{1-x}$ Bi $_x$ TiO $_3$ *Lead-Free* Ceramics, Integr. Ferroelectr. 166 (2015) 186–196. https://doi.org/10.1080/10584587.2015.1092629.

[19]   S. Islam, A. Siddika, N.A. Ahmed, N. Khatun, S.N. Rahman, Synthesis and Characterization of Bismuth Doped Barium Titanate, (2015) 6.

[20]   Z.C. Li, B. Bergman, Electrical properties and ageing characteristics of BaTiO3 ceramics doped by single dopants, J. Eur. Ceram. Soc. 25 (2005) 441–445. https://doi.org/10.1016/j.jeurceramsoc.2004.03.012.

[21]   F.Z. Krimech, S. Sayouri, T. Lamcharfi, Synthesis, structural and dielectric properties of Li-doped BaTiO3 nanopowders by sol-gel method, J. Ceram. Process. Res. 18 (2017) 536–542.

[22]   K. Limame, S. Sayouri, A. El Ghazouali, L. Hajji, T. Lamcharfi, B. Jaber, A. Housni, Diffuse Phase Transition, Relaxor Behavior and Anomalies in (Pb, La)TiO3 Ceramics, Ferroelectrics. 371 (2008) 68–81. https://doi.org/10.1080/00150190802394244.

[23]   H. Gatea, S. Jasim, Preparation and Characterization of Ba1-xSrxTiO3 by Sol-Gel Method, Asian J. Chem. 31 (2019) 186–190. https://doi.org/10.14233/ajchem.2019.21660.

[24]   M. Tihtih, J.F.M. Ibrahim, E. Kurovics, M. Abdelfattah, Study on the effect of Bi dopant on the structural and optical properties of BaTiO3 nanoceramics synthesized via sol-gel method, J. Phys. Conf. Ser. 1527 (2020) 012043. https://doi.org/10.1088/1742-6596/1527/1/012043.

[25]   X.P. Jiang, M. Zeng, K.W. Kowk, H.L.W. Chan, Dielectric and Ferroelectric Properties of Bi-Doped BaTiO3 Ceramics, Key Eng. Mater. 334–335 (2007) 977–980. https://doi.org/10.4028/www.scientific.net/KEM.334-335.977.

[26]   L. Yang, H. Qiu, L. Pan, Z. Guo, M. Xu, J. Yin, X. Zhao, Magnetic properties of BaTiO3 and BaTi1−xMxO3 (M=Co, Fe) nanocrystals by hydrothermal method, J. Magn. Magn. Mater. 350 (2014) 1–5. https://doi.org/10.1016/j.jmmm.2013.09.036.

[27] H. Liu, B. Cao, C. O'Connor, Intrinsic magnetism in BaTiO$_3$ with magnetic transition element dopants (Co, Cr, Fe) synthesized by sol-precipitation method, J. Appl. Phys. 109 (2011) 07B516. https://doi.org/10.1063/1.3556768.

[28] A. Rani, J. Kolte, P. Gopalan, Investigation on the structural, multiferroic and magnetoelectric properties of BaTi1-xNixO3 ceramics, Ceram. Int. 45 (2019) 5312–5320. https://doi.org/10.1016/j.ceramint.2018.11.229.

[29] F. Lin, D. Jiang, X. Ma, W. Shi, Influence of doping concentration on room-temperature ferromagnetism for Fe-doped BaTiO3 ceramics, J. Magn. Magn. Mater. 320 (2008) 691–694. https://doi.org/10.1016/j.jmmm.2007.08.008.

[30] A. Rani, J. Kolte, P. Gopalan, Structural, electrical, magnetic and magnetoelectric properties of Co-doped BaTiO3 multiferroic ceramics, Ceram. Int. 44 (2018) 16703–16711. https://doi.org/10.1016/j.ceramint.2018.06.098.

[31] S. Pandey, O. Parkash, D. Kumar, Structural, Dielectric and Impedance Spectroscopic Studies on Fe Doped BaTiO3, Trans. Indian Ceram. Soc. 77 (2018) 209–218. https://doi.org/10.1080/0371750X.2018.1526653.

[32] K.C. Verma, R.K. Kotnala, Multiferroic approach for Cr,Mn,Fe,Co,Ni,Cu substituted BaTiO3 nanoparticles, Mater. Res. Express. 3 (2016) 055006. https://doi.org/10.1088/2053-1591/3/5/055006.

[33] Z. Guo, L. Yang, H. Qiu, X. Zhan, J. Yin, L. Cao, STRUCTURAL, MAGNETIC AND DIELECTRIC PROPERTIES OF Fe-DOPED BaTiO3 SOLIDS, Mod. Phys. Lett. B. 26 (2012) 1250056. https://doi.org/10.1142/S021798491250056X.

[34] P.P. Khirade, S.D. Birajdar, A.V. Raut, K.M. Jadhav, Effect of Fe – substitution on phase transformation, optical, electrical and dielectrical properties of BaTiO3 nanoceramics synthesized by sol-gel auto combustion method, J. Electroceramics. 37 (2016) 110–120. https://doi.org/10.1007/s10832-016-0044-z.

[35] N. Gouitaa, T. Lamcharfi, L. Bouayad, F. Abdi, M.N. Bennani, Structural and dielectric properties of Ba0.95Bi0.05Ti1-xFexO3ceramics at x=0.0, 0.1 and 0.2 prepared by solid state method, Mediterr. J. Chem. 8 (2019) 220–227. https://doi.org/10.13171/mjc8319050305ng.

[36] W. Yansen, D. Kim, K.J. Parwanta, C. Liu, B.W. Lee, Rietveld analysis and multiferroic properties of Fe doped Ba0.95Bi0.05TiO3 ceramics, Curr. Appl. Phys. 15 (2015) 120–123. https://doi.org/10.1016/j.cap.2014.12.001.

[37] Y. Wang, Y. Pu, X. Li, H. Zheng, Z. Gao, Investigation of relaxation phenomena in (Ba,Bi)(Ti,Fe)O3 ceramics by complex impedance spectroscopy, J. Mater. Sci. Mater. Electron. 27 (2016) 12251–12257. https://doi.org/10.1007/s10854-016-5382-8.

[38] H. Yamamoto, H. Kumehara, R. Takeuchi, H. Nishio, Magnetic Properties of Sr-M Ferrite Fine Particles, J. Phys. IV. 07 (1997) C1-536. https://doi.org/10.1051/jp4:19971219.

[39] S. Islam, S.A. Satter, N. Khatun, M.S. Hossain, S.F.U. Farhad, P. Bala, S. Tabassum, A. Siddika, Investigation of Structural, Dielectric and Electrical Properties of Barium Titanate Ceramics Co-Doped with Bismuth and Yttrium, J. Mol. Eng. Mater. 07 (2019) 1950006. https://doi.org/10.1142/S2251237319500060.

[40] N. Masó, H. Beltrán, E. Cordoncillo, P. Escribano, A.R. West, Electrical properties of Fe-doped BaTiO$_3$, J Mater Chem. 16 (2006) 1626–1633. https://doi.org/10.1039/B515834F.

[41] R.D. Shannon, Revised effective ionic radii and systematic studies of interatomic distances in halides and chalcogenides, Acta Crystallogr. Sect. A. 32 (1976) 751–767. https://doi.org/10.1107/S0567739476001551.

[42] F. Craciun, M. Cernea, V. Fruth, M. Zaharescu, I. Atkinson, N. Stanica, L.C. Tanase, L. Diamandescu, A. Iuga, C. Galassi, Novel multiferroic

(Pb1−3x/2Ndx)(Ti0.98−yFeyMn0.02)O3 ceramics with coexisting ferroelectricity and ferromagnetism at ambient temperature, Mater. Des. 110 (2016) 693–704. https://doi.org/10.1016/j.matdes.2016.08.046.

[43]   N.S. Kumar, R.P. Suvarna, K.C.B. Naidu, Multiferroic Nature of Microwave-Processed and Sol-Gel Synthesized NanoPb1-xCoxTiO3 (x = 0.2–0.8) Ceramics, Cryst. Res. Technol. 53 (2018) 1800139. https://doi.org/10.1002/crat.201800139.

[44]   P. Scherrer, Bestimmung der Größe und der inneren Struktur von Kolloidteilchen mittels Röntgenstrahlen, Nachrichten Von Ges. Wiss. Zu Gött. Math.-Phys. Kl. 1918 (1918) 98–100. https://eudml.org/doc/59018 (accessed November 3, 2022).

[45]   A. Monshi, M.R. Foroughi, M.R. Monshi, Modified Scherrer Equation to Estimate More Accurately Nano-Crystallite Size Using XRD, World J. Nano Sci. Eng. 2 (2012) 154–160. https://doi.org/10.4236/wjnse.2012.23020.

[46]   D. Kothandan, R. Jeevan Kumar, K. Chandra Babu Naidu, Barium titanate microspheres by low temperature hydrothermal method: studies on structural, morphological, and optical properties, J. Asian Ceram. Soc. 6 (2018) 1–6. https://doi.org/10.1080/21870764.2018.1439607.

[47]   D. Balzar, H. Ledbetter, Voigt-function modeling in Fourier analysis of size- and strain-broadened X-ray diffraction peaks, J. Appl. Crystallogr. 26 (1993) 97–103. https://doi.org/10.1107/S0021889892008987.

[48]   E. Prince, Accuracy in powder diffraction II, (n.d.) 248.

[49]   K. Chandra Babu Naidu, W. Madhuri, Effect of Nonmagnetic Zn2+ Cations on Initial Permeability of Microwave-Treated NiMg Ferrites, Int. J. Appl. Ceram. Technol. 13 (2016) 1090–1095. https://doi.org/10.1111/ijac.12571.

[50]   A. Shrivastava, S. Bisen, M. Khan, P. Sharma, A. Mishra, Synthesis and structural study of Cr-doped BaTiO3 by x-ray diffraction technique and Williamson-Hall and size strain plot methods, AIP Conf. Proc. 2100 (2019) 020166. https://doi.org/10.1063/1.5098720.

[51]   M. Khan, A. Mishra, J. Shukla, P. Sharma, X-ray analysis of BaTiO3 ceramics by Williamson-Hall and size strain plot methods, AIP Conf. Proc. 2100 (2019) 020138. https://doi.org/10.1063/1.5098692.

[52]   Z.V. Ooi, A.A. Saif, A Study on Er3+ Substitution in Sol-gel BaTiO3 Thin Films Using X-ray Line Profile Analysis, Mater. Sci. 23 (2017) 193–199. https://doi.org/10.5755/j01.ms.23.3.16225.

[53]   M.M. Vijatović, B.D. Stojanović, J.D. Bobić, T. Ramoska, P. Bowen, Properties of lanthanum doped BaTiO3 produced from nanopowders, Ceram. Int. 36 (2010) 1817–1824. https://doi.org/10.1016/j.ceramint.2010.03.010.

[54]   Y. Slimani, A. Selmi, E. Hannachi, M.A. Almessiere, M. Mumtaz, A. Baykal, I. Ercan, Study of tungsten oxide effect on the performance of BaTiO3 ceramics, J. Mater. Sci. Mater. Electron. 30 (2019) 13509–13518. https://doi.org/10.1007/s10854-019-01718-x.

[55]   X. Jin, D. Sun, M. Zhang, Y. Zhu, J. Qian, Investigation on FTIR spectra of barium calcium titanate ceramics, J. Electroceramics. 22 (2009) 285–290. https://doi.org/10.1007/s10832-007-9402-1.

[56]   J. Cao, Y. Ji, C. Tian, Z. Yi, Synthesis and enhancement of visible light activities of nitrogen-doped BaTiO3, J. Alloys Compd. 615 (2014) 243–248. https://doi.org/10.1016/j.jallcom.2014.07.008.

[57]   R. Ravanamma, K. Muralidhara Reddy, K. Venkata Krishnaiah, N. Ravi, Structure and morphology of yttrium doped barium titanate ceramics for multi-layer capacitor applications, Mater. Today Proc. 46 (2021) 259–262. https://doi.org/10.1016/j.matpr.2020.07.646.

[58]   Y.T. Wu, X.F. Wang, C.L. Yu, E.Y. Li, Preparation and Characterization of Barium Titanate (BaTiO3) Nano-Powders by Pechini Sol-Gel Method, Mater. Manuf. Process. 27 (2012) 1329–1333. https://doi.org/10.1080/10426914.2012.663148.

[59]   M.K. Adak, S.J. Mahato, U. Mahato, U.R. Gorai, S. Mondal, S. Kar, P. Dhak, D. Dhak, Investigation of energy storage and electrical properties of modified BaTiO3 doped by BaBi2Nb2O9 nano crystalline ceramics, Phys. B Condens. Matter. 578 (2020) 411885. https://doi.org/10.1016/j.physb.2019.411885.

[60]   K. Nakamoto, Infrared and Raman Spectra of Inorganic and Coordination Compounds, in: Handb. Vib. Spectrosc., John Wiley & Sons, Ltd, 2006. https://doi.org/10.1002/0470027320.s4104.

[61]   K. Zarel', M.S. Sadjadi, M. Enhessari, S. Khanahmadzadeh, Synthesis and Characterization of PbTiO3 Nanopowders by Citric Acid Gel Method, (2009) 4.

[62]   S. Kazi, F. Savanur, S.S. Kakati, S. Mathad, P. Jeergal, A. Pujar, C. Hiremath, S. Galgali, M. Rendale, R. Pujar, Sintering Temperature Dependent Structural and Mechanical Studies of BaxPb1 − xTiO3 Ferroelectrics, J. Nano- Electron. Phys. 12 (2020) 04018–1. https://doi.org/10.21272/jnep.12(4).04018.

[63]   M.K. Adak, D. Dhak, Assessment of strong relaxation on BaTiO3 modified by Mn2+ and Pr3+, K+ at A− and B− site respectively, Mater. Res. Express. 6 (2019) 125082. https://doi.org/10.1088/2053-1591/ab5ae9.

[64]   A. Mishra, N. Mishra, Iron-doped BaTiO3: Influence of iron on physical properties, Int. J. Mater. Sci. Appl. 1 (2012) 14. https://doi.org/10.11648/j.ijmsa.20120101.13.

[65]   A. Abdel Aal, T.R. Hammad, M. Zawrah, I.K. Battisha, A.B. Abou Hammad, FTIR Study of Nanostructure Perovskite BaTiO $_3$ Doped with Both Fe $^{3+}$ and Ni $^{2+}$ Ions Prepared by Sol-Gel Technique, Acta Phys. Pol. A. 126 (2014) 1318–1321. https://doi.org/10.12693/APhysPolA.126.1318.

[66]   P.P. Khirade, S.D. Birajdar, A.V. Raut, K.M. Jadhav, Multiferroic iron doped BaTiO3 nanoceramics synthesized by sol-gel auto combustion: Influence of iron on physical properties, Ceram. Int. 10 (2016) 12441–12451. https://doi.org/10.1016/j.ceramint.2016.05.021.

[67]   Q. Zhang, J. Zhai, Q. Ben, X. Yu, X. Yao, Enhanced microwave dielectric properties of Ba $_{0.4}$ Sr $_{0.6}$ TiO $_3$ ceramics doping by metal Fe powders, J. Appl. Phys. 112 (2012) 104104. https://doi.org/10.1063/1.4766276.

[68]   C.J. Johnson, SOME DIELECTRIC AND ELECTRO-OPTIC PROPERTIES OF BaTiO3 SINGLE CRYSTALS, Appl. Phys. Lett. 7 (1965) 221–223. https://doi.org/10.1063/1.1754387.

[69]   P. Gupta, P.K. Mahapatra, R.N.P. Choudhary, Investigation on structural and electrical properties of Co and W modified BaTiO3, Ceram. Int. 45 (2019) 22862–22871. https://doi.org/10.1016/j.ceramint.2019.07.329.

[70]   N. Gouitaa, L. Taj-dine, M. Bouayad, A. Farid, M. Haddad, Rietveld refinement and diffuse phases transition of Ba1-XBixTi0.8Fe0.2O3 ceramics at x=0.00, 0.05, 0.10 and 0.15 prepared by solid state method., In Review, 2020. https://doi.org/10.21203/rs.3.rs-21117/v1.

[71]   Diffuse and relaxor phase transitions of Ba 0.95Bi 0.05Ti 1-xFe xO3 ceramics at x=0.00 to 1.00 of Fe content, prepared by solid state method - IOPscience, (n.d.). https://iopscience.iop.org/article/10.1088/1757-899X/1160/1/012006/meta (accessed November 3, 2022).

[72]   F. Bourguiba, Ah. Dhahri, T. Tahri, J. Dhahri, N. Abdelmoula, K. Taibi, E.K. Hlil, Structure properties and relaxor characteristics of the phases transformation in BaTi0.5(Fe0.33Mo0.17)O3 perovskite ceramic, J. Alloys Compd. 675 (2016) 174–182. https://doi.org/10.1016/j.jallcom.2016.03.016.

[73]   L. Tawee, P. Jaita, R. Sanjoom, K. Pengpat, S. Eitssayeam, T. Tunkasiri, G. Rujijanagul, S.J. Mile, Dielectric properties of Ba1-xSrx(Fe0.5Ta0.5)O3 giant dielectric ceramics, Ferroelectrics. 511 (2017) 52–61. https://doi.org/10.1080/00150193.2017.1333372.

[74]   N. Raghuram, T. Subba Rao, K. Chandra Babu Naidu, Electrical and impedance spectroscopy properties of hydrothermally synthesized Ba0.2Sr0.8-yLayFe12O19 (y = 0.2–0.8) nanorods, Ceram. Int. 46 (2020) 5894–5906. https://doi.org/10.1016/j.ceramint.2019.11.042.

[75]   PRIYANKA, A.K. JHA, Electrical characterization of zirconium substituted barium titanate using complex impedance spectroscopy, Bull. Mater. Sci. 36 (2013) 135–141. https://doi.org/10.1007/s12034-013-0420-0.

[76]   P.S. Sahoo, A. Panigrahi, S.K. Patri, R.N.P. Choudhary, Structural and impedance properties of Ba5DyTi3V7O30, J. Mater. Sci. Mater. Electron. 20 (2009) 565–570. https://doi.org/10.1007/s10854-008-9766-2.

[77]   N.S. Kumar, R.P. Suvarna, K.C. Babu Naidu, Microwave heated lead cobalt titanate nanoparticles synthesized by sol-gel technique: Structural, morphological, dielectric, impedance and ferroelectric properties, Mater. Sci. Eng. B. 242 (2019) 23–30. https://doi.org/10.1016/j.mseb.2019.03.005.

[78]   D.S. Kumar, K.C.B. Naidu, M.M. Rafi, K.P. Nazeer, A.A. Begam, G.R. Kumar, Structural and dielectric properties of superparamagnetic iron oxide nanoparticles (SPIONs) stabilized by sugar solutions, Mater. Sci.-Pol. 36 (2018) 123–133. https://doi.org/10.1515/msp-2018-0017.

[79]   A. Selmi, M. Khelifi, H. Rahmouni, R. M'nassri, K. Khirouni, N. Chniba Boudjada, A. Cheikhrouhou, Electrical conductivity analysis and magnetic properties of Pr0.7Ca0.3Mn0.95Co0.05O3 oxide, J. Mater. Sci. Mater. Electron. 28 (2017) 1901–1908. https://doi.org/10.1007/s10854-016-5742-4.

[80]   Z. Chchiyai, F. El Bachraoui, Y. Tamraoui, L. Bih, A. Lahmar, A. Faik, J. Alami, B. Manoun, Synthesis, structural refinement and physical properties of novel perovskite ceramics Ba1-xBixTi1-xMnxO3 (x = 0.3 and 0.4), Mater. Chem. Phys. 262 (2021) 124302. https://doi.org/10.1016/j.matchemphys.2021.124302.

[81]   M. Nadeem, M.J. Akhtar, M.N. Haque, Increase of grain boundary resistance with time by impedance spectroscopy in La0.50Ca0.50MnO3+δ at 77 K, Solid State Commun. 145 (2008) 263–266. https://doi.org/10.1016/j.ssc.2007.11.013.

[82]   M. Shah, M. Nadeem, M. Idrees, M. Atif, M.J. Akhtar, Change of conduction mechanism in the impedance of grain boundaries in Pr0.4Ca0.6MnO3, J. Magn. Magn. Mater. 332 (2013) 61–66. https://doi.org/10.1016/j.jmmm.2012.12.015.

[83]   Y. Moualhi, R. M'nassri, M.M. Nofal, H. Rahmouni, A. Selmi, M. Gassoumi, N. Chniba-Boudjada, K. Khirouni, A. Cheikhrouhou, Magnetic properties and impedance spectroscopic analysis in Pr0.7Ca0.3Mn0.95Fe0.05O3 perovskite ceramic, J. Mater. Sci. Mater. Electron. 31 (2020) 21046–21058. https://doi.org/10.1007/s10854-020-04617-8.

[84]   R. Lahouli, J. Massoudi, M. Smari, H. Rahmouni, K. Khirouni, E. Dhahri, L. Bessais, Investigation of annealing effects on the physical properties of Ni 0.6 Zn 0.4 Fe 1.5 Al 0.5 O 4 ferrite, RSC Adv. 9 (2019) 19949–19964. https://doi.org/10.1039/C9RA02238D.

[85]   A.K. Jonscher, The `universal' dielectric response, Nature. 267 (1977) 673–679. https://doi.org/10.1038/267673a0.

[86]   A. Ghosh, Frequency-dependent conductivity in bismuth-vanadate glassy semiconductors, Phys. Rev. B. 41 (1990) 1479–1488. https://doi.org/10.1103/PhysRevB.41.1479.

[87]   N.F. Mott, E.A. Davis, N.F. Mott, E.A. Davis, Electronic Processes in Non-Crystalline Materials, Oxford University Press, Oxford, New York, 2012.

[88]   H. Rahmouni, B. Cherif, M. Baazaoui, K. Khirouni, Effects of iron concentrations on the electrical properties of La0.67Ba0.33Mn1−xFexO3, J. Alloys Compd. 575 (2013) 5–9. https://doi.org/10.1016/j.jallcom.2013.04.077.

[89]   R. Moussi, A. Bougoffa, A. Trabelsi, E. Dhahri, M.P.F.Graça, M.A. Valente, R. Barille, Effect of Sr-substitution on structure, dielectric relaxation and conduction phenomenon of BaTiO3 perovskite material, J. Mater. Sci. Mater. Electron. 32 (2021) 11453–11466. https://doi.org/10.1007/s10854-021-05604-3.

[90]   S. Yoshioka, S. Tajima, Y. Aso, S. Kojima, Inactivation and Aggregation of β-Galactosidase in Lyophilized Formulation Described by Kohlrausch-Williams-Watts Stretched Exponential Function, Pharm. Res. 20 (2003) 1655–1660. https://doi.org/10.1023/A:1026151721212.

[91]   M. Ben Bechir, K. Karoui, M. Tabellout, K. Guidara, A. Ben Rhaiem, Alternative current conduction mechanisms of organic-inorganic compound [N(CH3)3H]2ZnCl4, J. Appl. Phys. 115 (2014) 153708. https://doi.org/10.1063/1.4871662.

[92]   C.G. Koops, On the Dispersion of Resistivity and Dielectric Constant of Some Semiconductors at Audiofrequencies, Phys. Rev. 83 (1951) 121–124. https://doi.org/10.1103/PhysRev.83.121.

[93]   K. Chandra Babu Naidu, M. Wuppulluri, Ceramic Nanoparticle Synthesis at Lower Temperatures for LTCC and MMIC Technologies, IEEE Trans. Magn. 54 (2018) 2855663. https://doi.org/10.1109/TMAG.2018.2855663.

[94]   T.V. Sagar, T.S. Rao, K.C.B. Naidu, Effect of calcination temperature on optical, magnetic and dielectric properties of Sol-Gel synthesized Ni0.2Mg0.8-xZnxFe2O4 (x = 0.0–0.8), Ceram. Int. 46 (2020) 11515–11529. https://doi.org/10.1016/j.ceramint.2020.01.178.

[95]   C.B.N. Kadiyala, S. Dastagiri, Induced dielectric behavior in high dense AlxLa1-xTiO3 (x = 0.2 - 0.8) nanospheres, J. Mater. Sci. Mater. Electron. 30 (2019). https://doi.org/10.1007/s10854-019-02409-3.

[96]   M.S. Panday, M. Vinoth, S. Surendhiran, V. Rajendran, P.S. Menon, Investigation on electrical conductivity of strontium (Sr2+) influenced CaTi0.8Fe0.2O3 polycrystalline perovskite, in: 2016 IEEE Int. Conf. Semicond. Electron. ICSE, 2016: pp. 192–195. https://doi.org/10.1109/SMELEC.2016.7573624.

[97]   M. Padhy, S.K. Dehury, R.N.P. Choudhary, P.G.R. Achary, Structural, dielectric, thermal and electrical characteristics of lead-free double perovskite: BiHoZnCeO6, Appl. Phys. A. 126 (2020) 655. https://doi.org/10.1007/s00339-020-03852-4.

LIST OF FIGURES
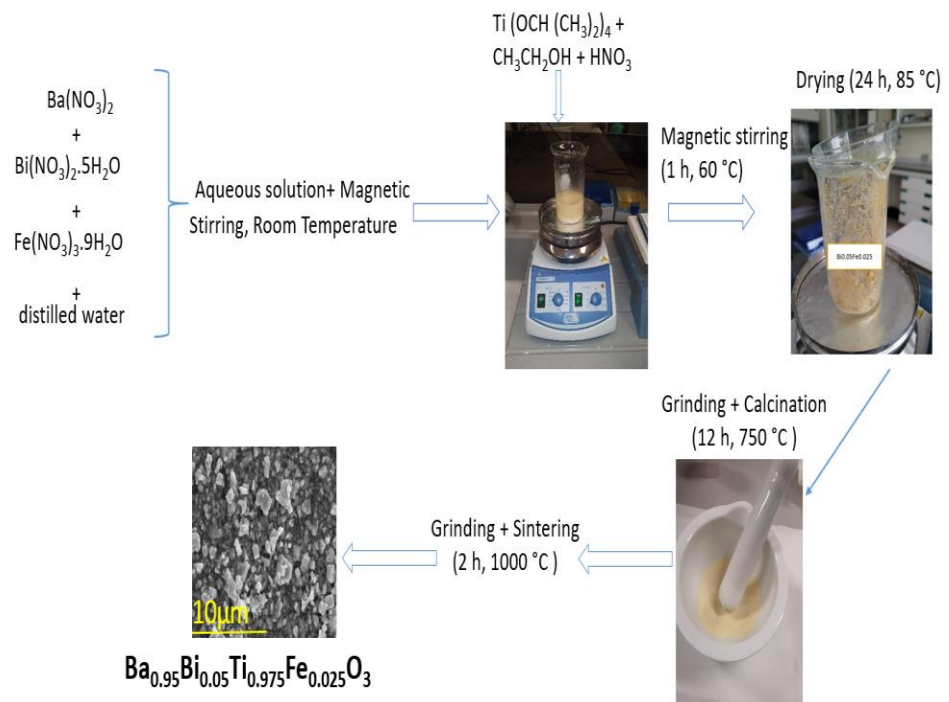
Figure 1: *The synthesis process of $Ba_{0.95}Bi_{0.05}Ti_{1-x}Fe_xO_3$ (x= 0.025, 0.050 and 0.075)*
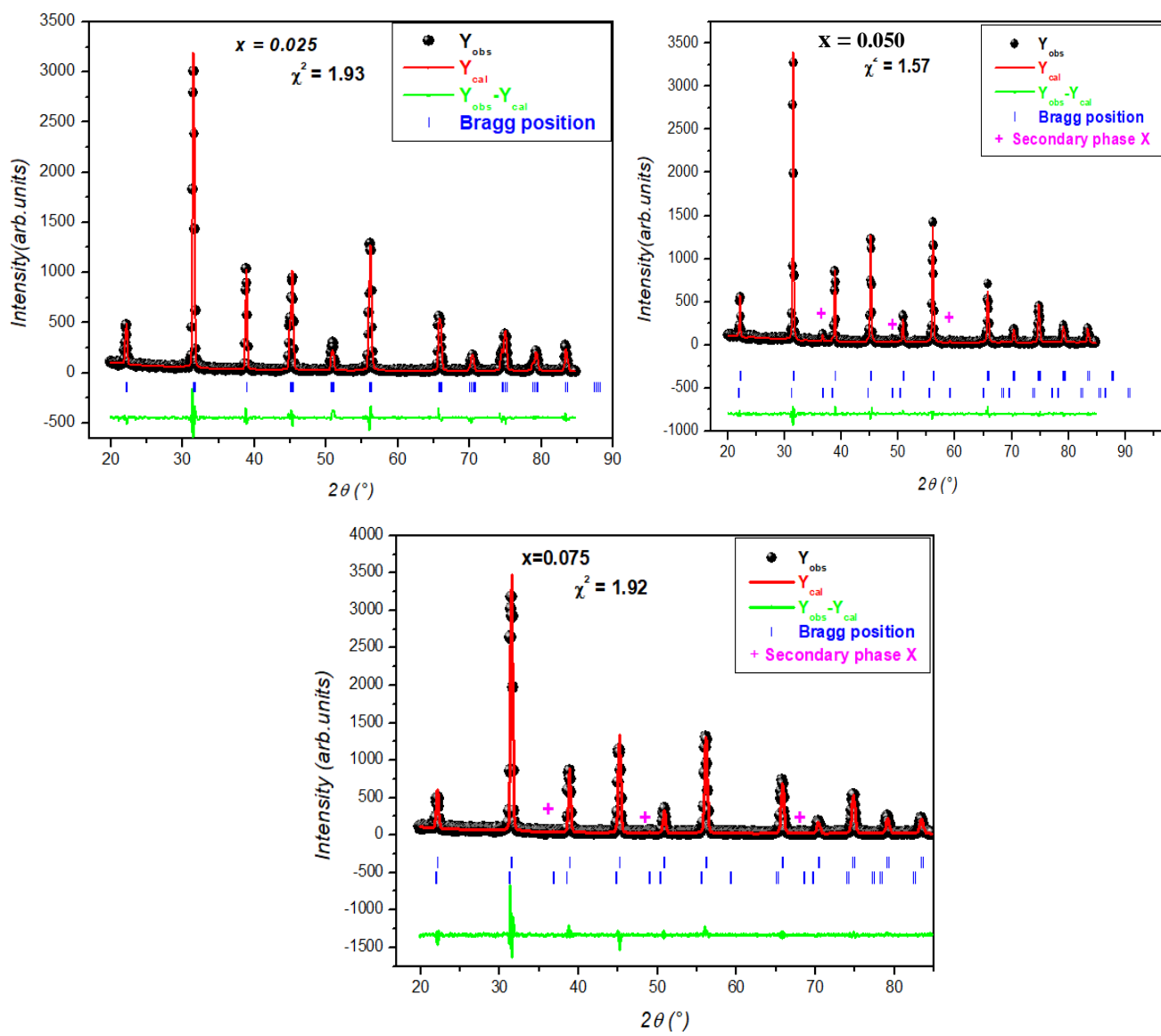
Figure 2: X-ray diffraction patterns (XRD) of Ba$_{0.95}$Bi$_{0.05}$Ti$_{1-x}$Fe$_x$O$_3$
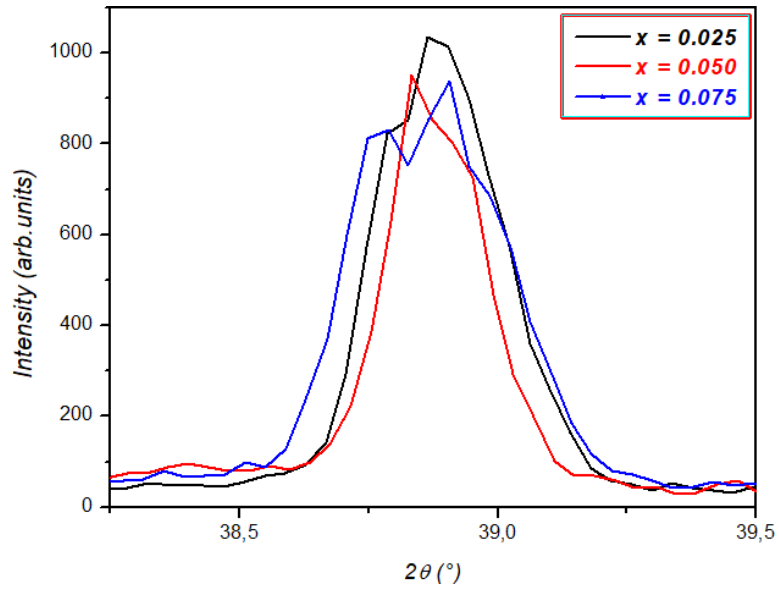
Figure 3: Variation of the peak (111) of $Ba_{0.95}Bi_{0.05}Ti_{1-x}Fe_xO_3$
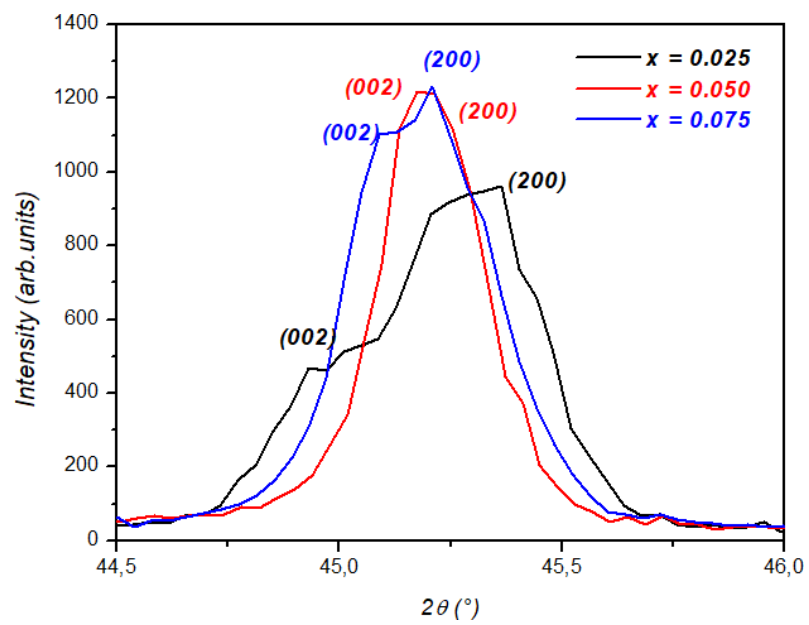
Figure 4: Splitting of the peaks (002) and (200) of $Ba_{0.95}Bi_{0.05}Ti_{1-x}Fe_xO_3$
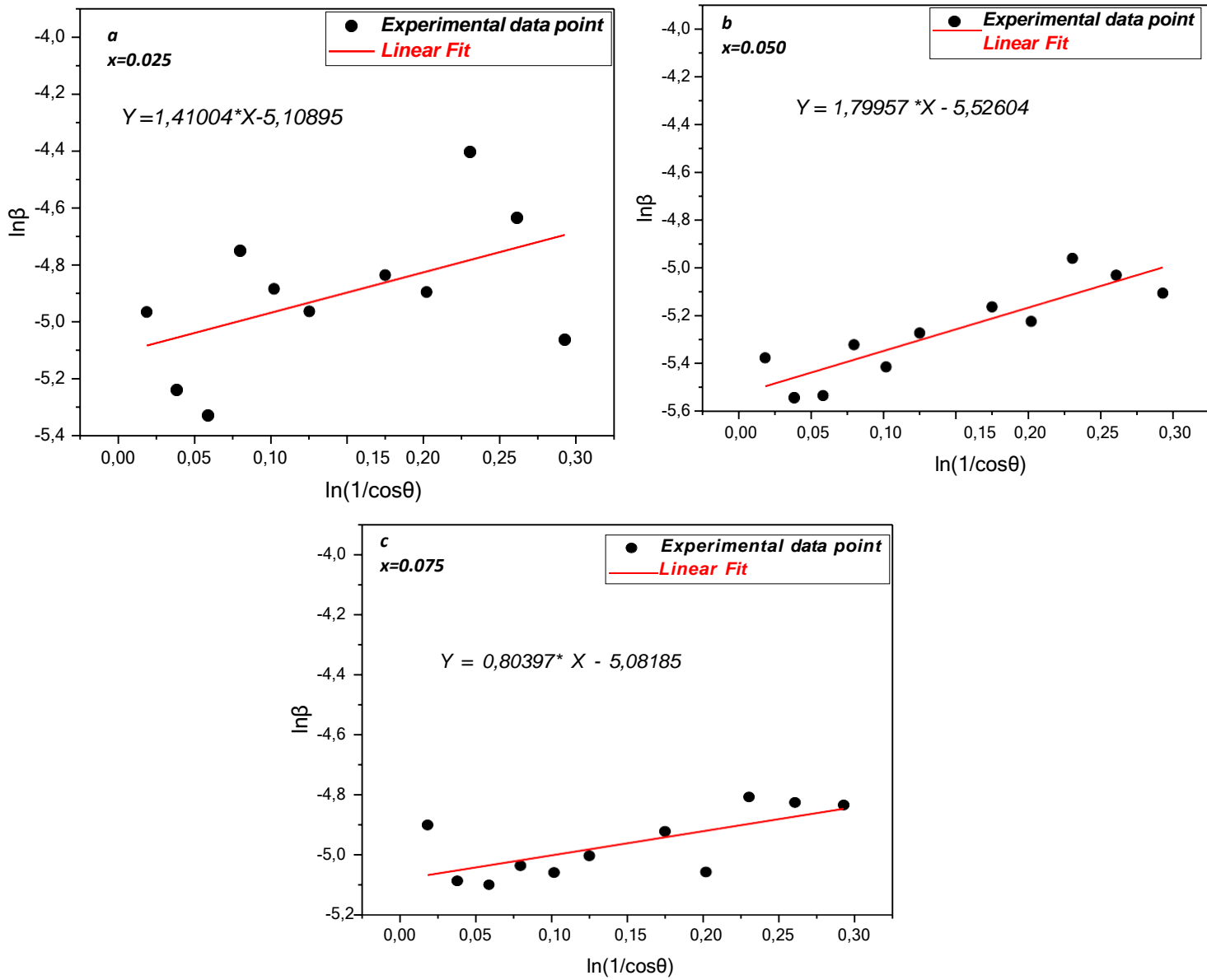
Figure 5: Modified Scherrer equation representation of Ba$_{0.95}$Bi$_{0.05}$Ti$_{1-x}$Fe$_x$O3 for (a) x=0.025, (b) x=0.050 and (c) x=0.075
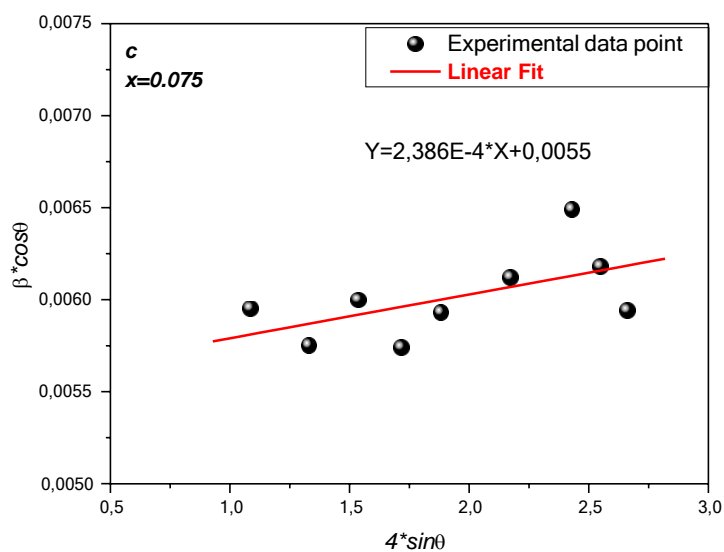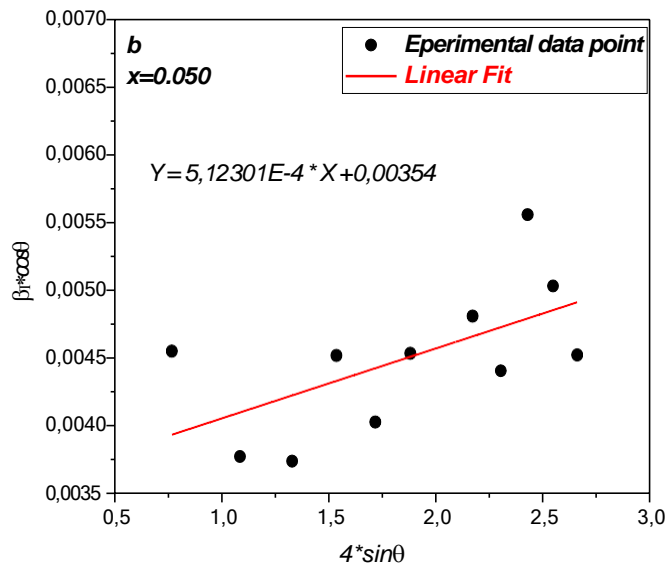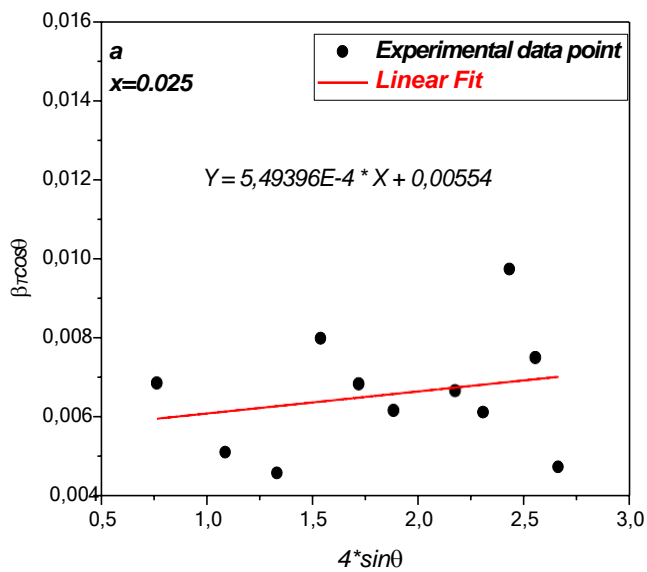
Figure 6: Williamson-Hall plot for Ba0.95Bi0.05Ti1-xFexO3 for (a) x=0.025, (b) x=0.050 and (c) x=0.075
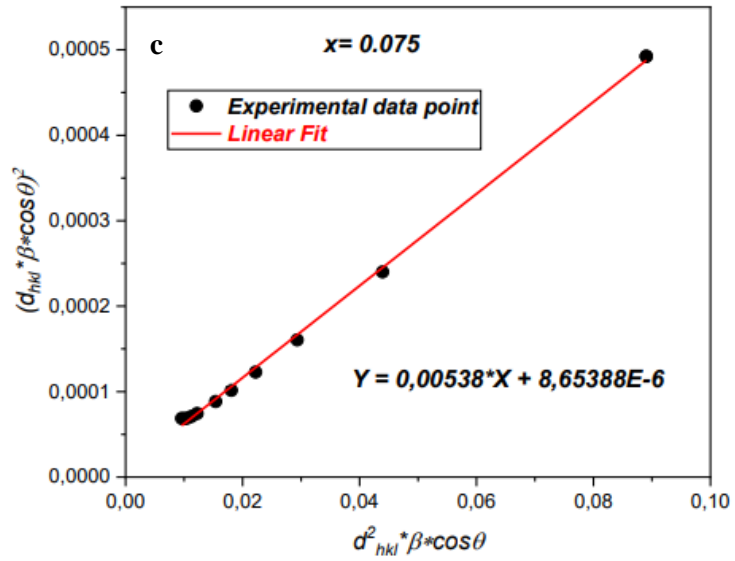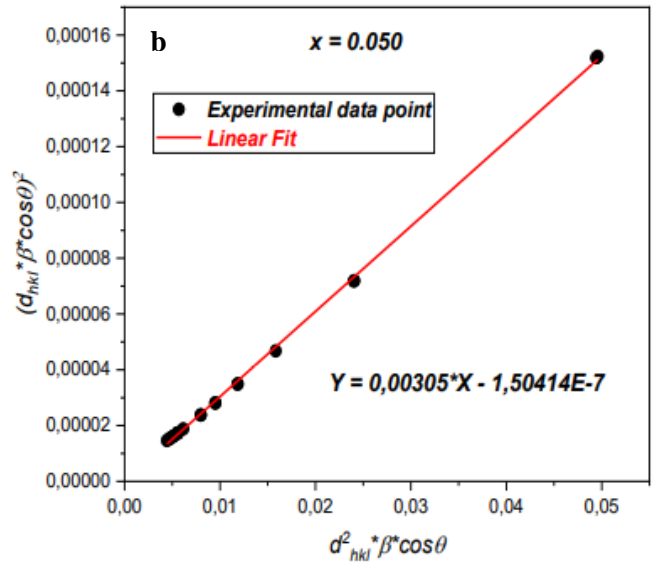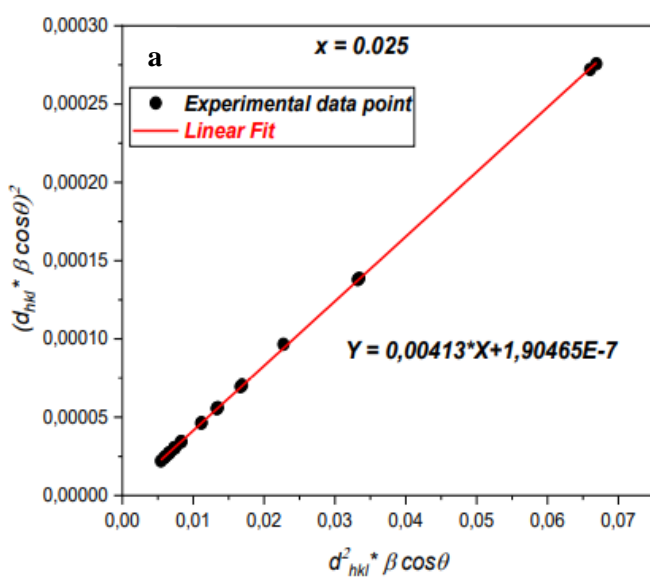
Figure 7: SSP methods for Ba0,95Bi0,05Ti1-xFexO3 with (a) x=0.025, (b) x=0.050 and (c) x=0.075
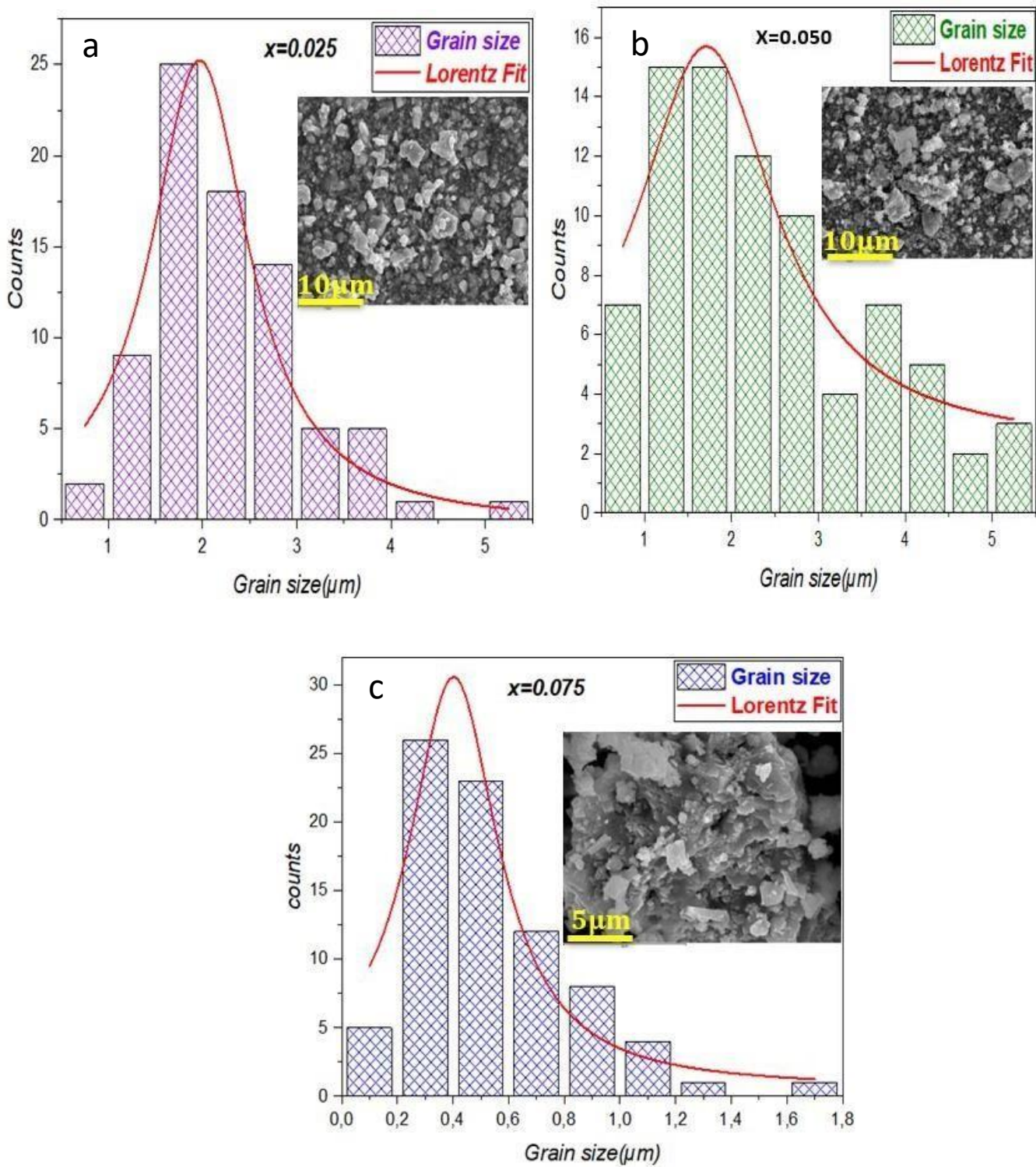
Figure 8: SEM micrographs and particle Size distribution of $Ba_{0.95}Bi_{0.05}Ti_{1-x}Fe_xO_3$ with *(a) x=0.025, (b) x=0.050 and (c) x=0.075*
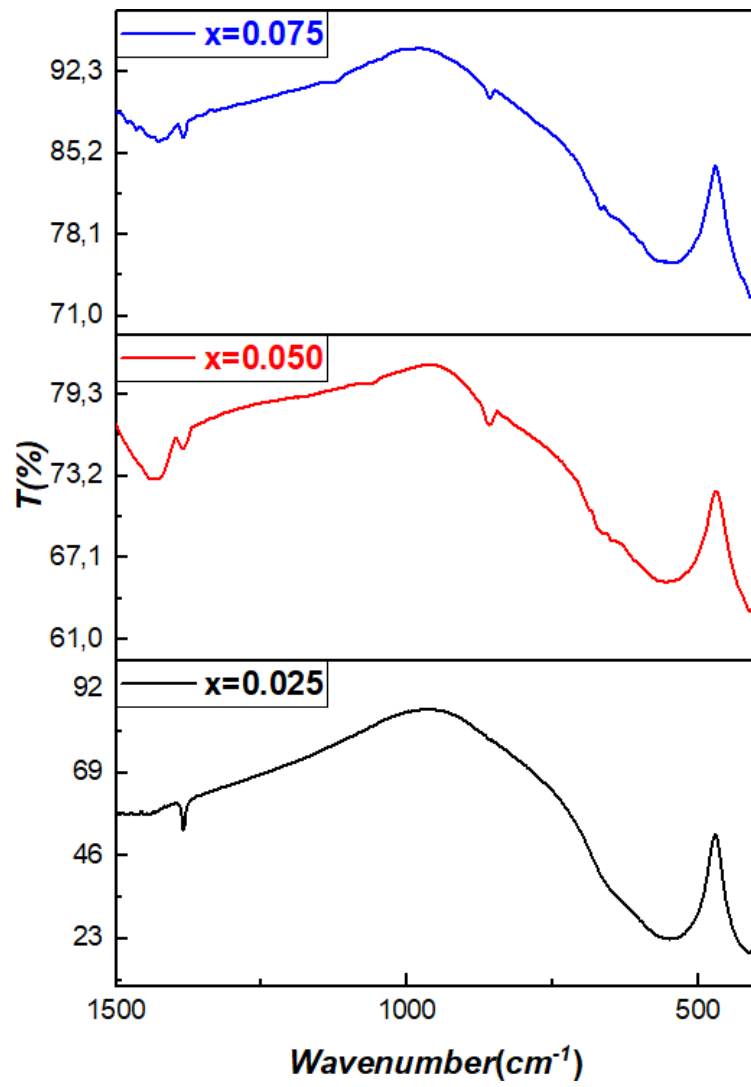
Figure 9: FTIR spectra of $Ba_{0.95}Bi_{0.05}Ti_{1-x}Fe_xO_3$
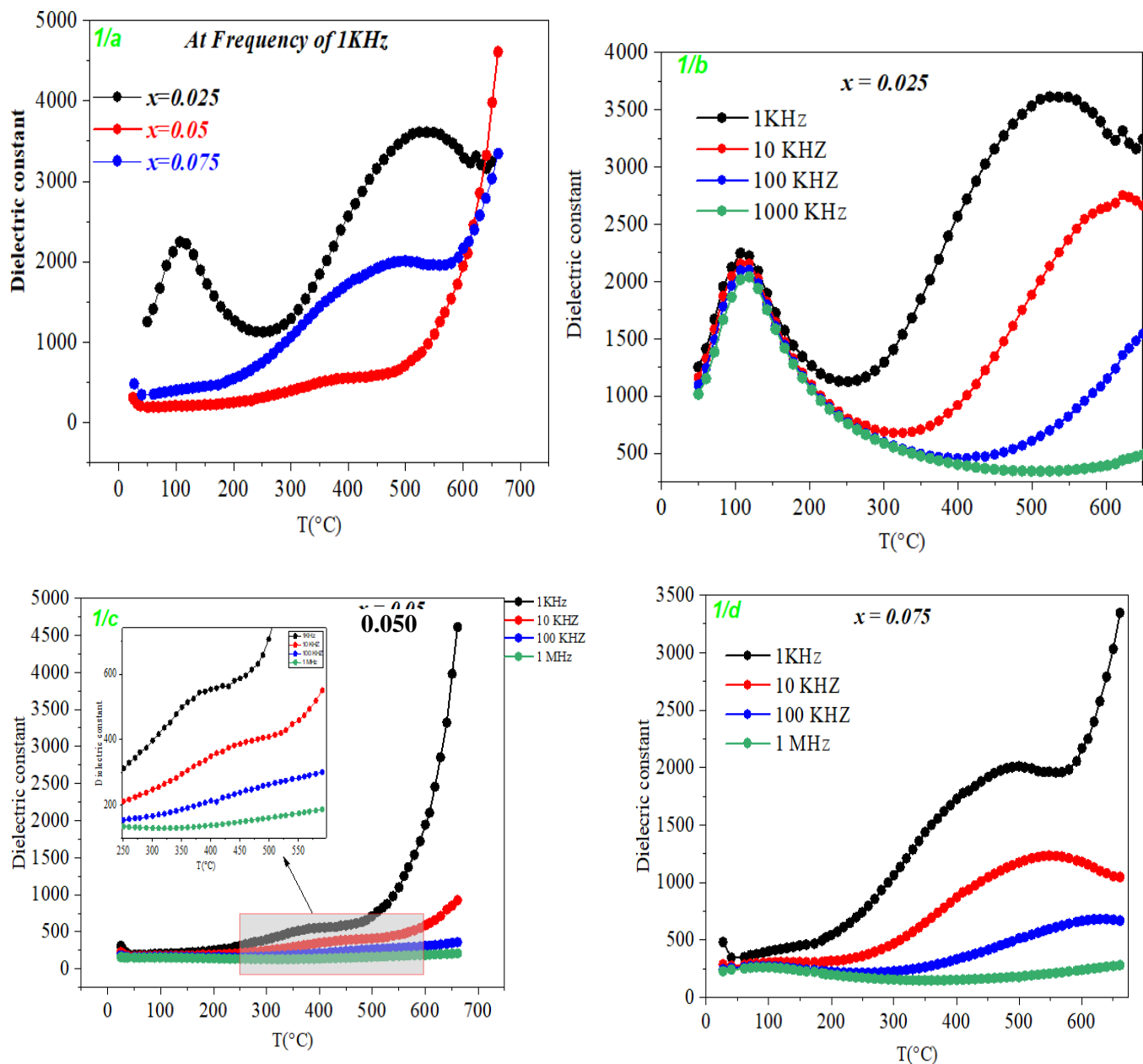
Figure 10:The evolution of the dielectric constant as a function of temperature of Ba$_{0.95}$Bi$_{0.05}$Ti$_{1-x}$Fe$_x$O$_3$: 1/a evolution of dielectric constant at 1KHz, 1/b variation of dielectric constant for x=0.025, 1/c variation of dielectric constant for x=0.050, 1/d variation of dielectric constant for x=0.075
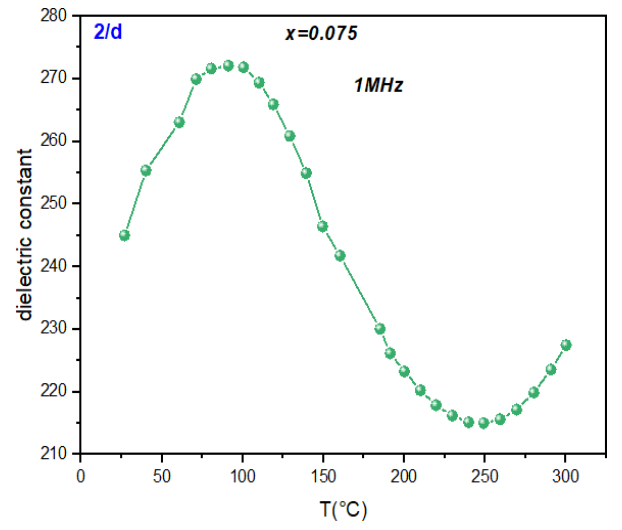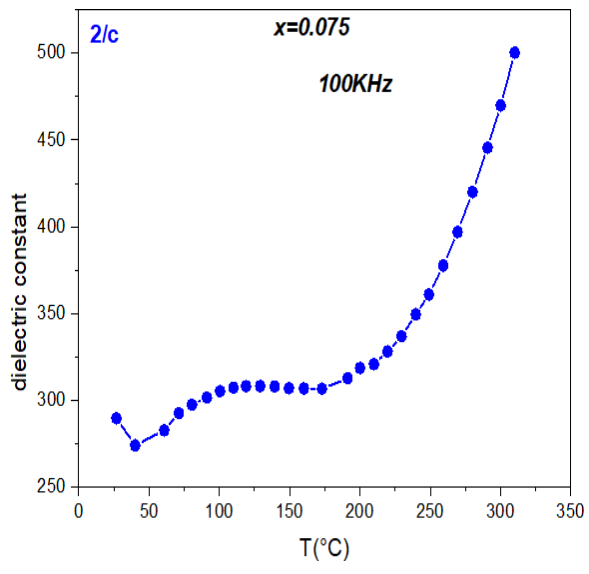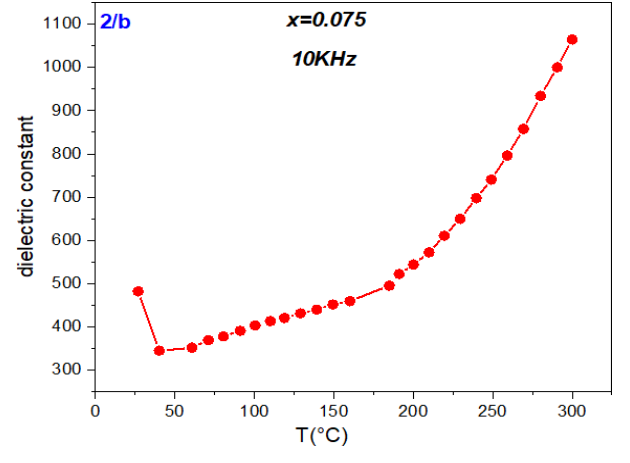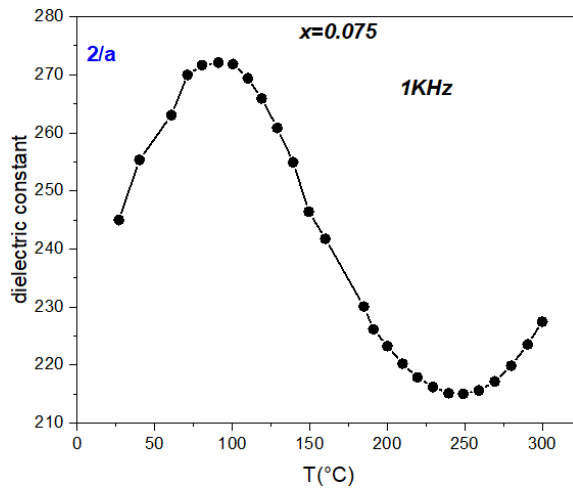
Figure 11: Enlarged loops for each frequency of Ba$_{0.95}$Bi$_{0.05}$Ti$_{1-x}$Fe$_x$O$_3$ with x=0.075
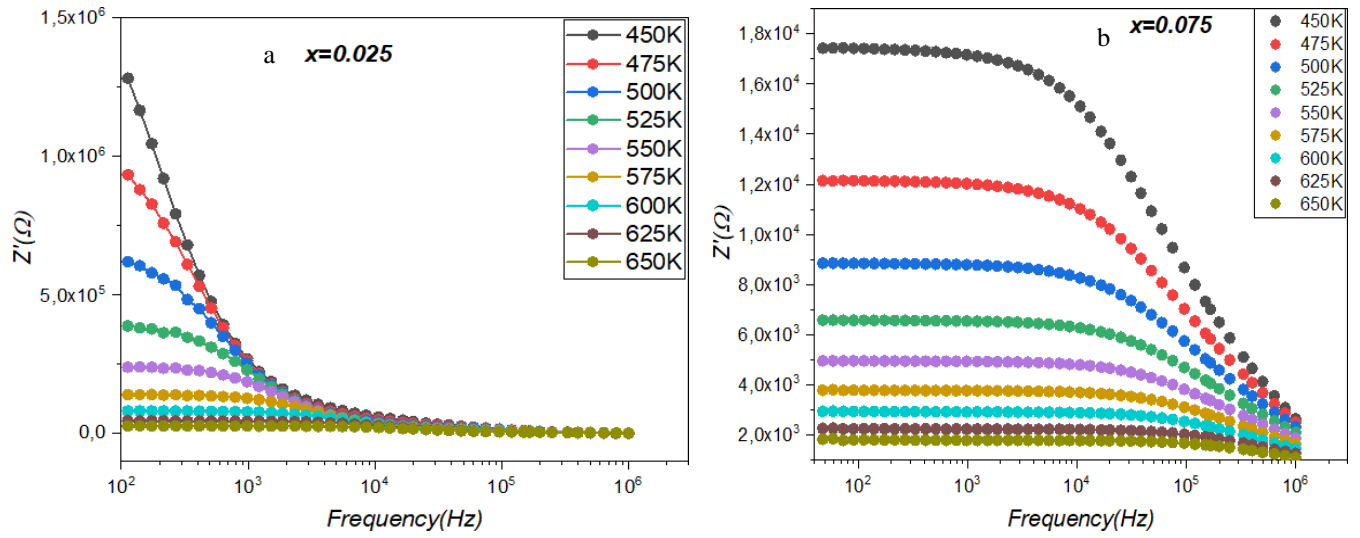
Figure 12: Variation of reel part of impedance for both samples with (a) x=0.025 and (b) x= 0.075
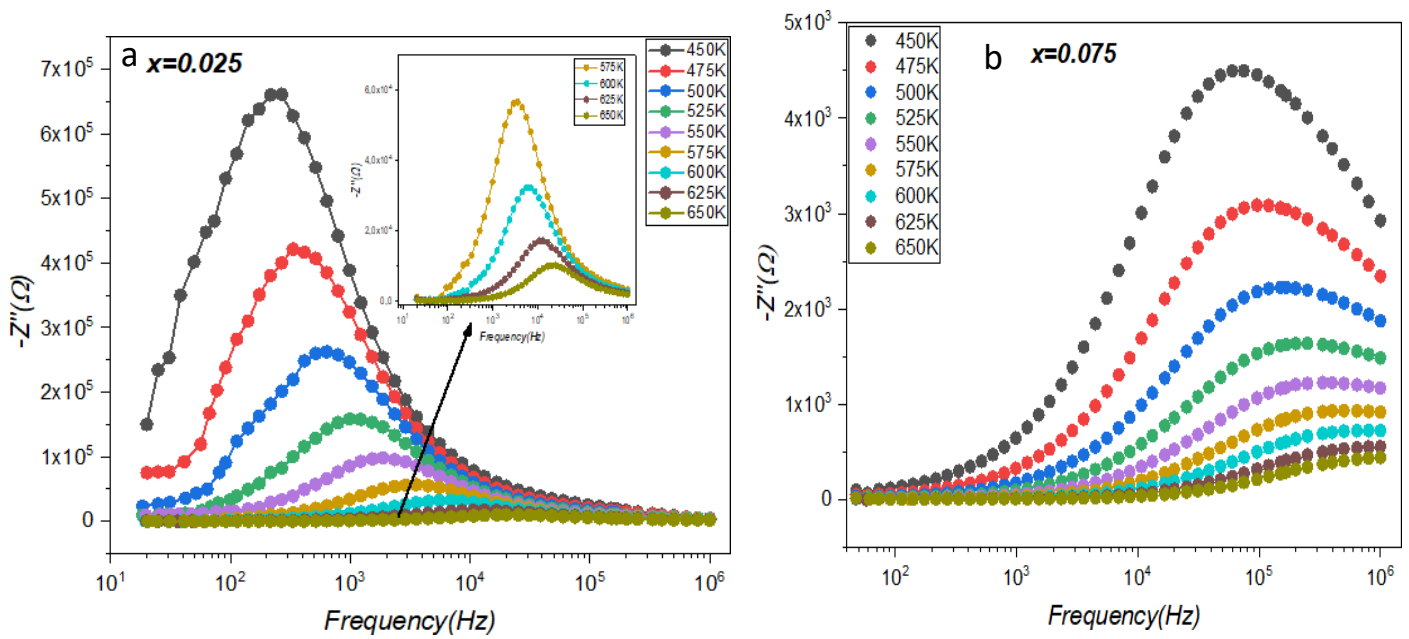
Figure 13: Variation of imaginary part of impedance for both samples with (a) x=0.025 and (b) x= 0.075
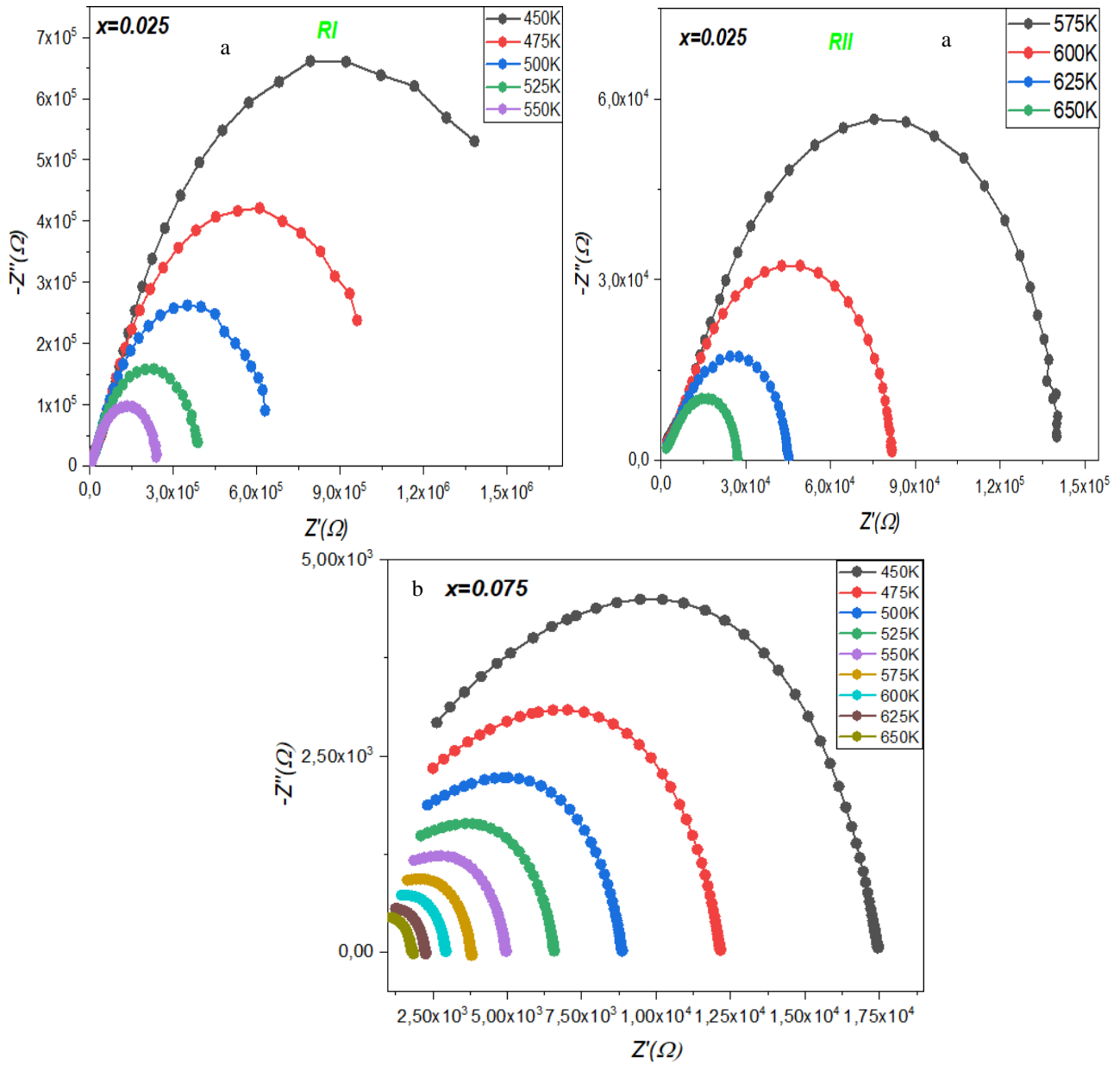
Figure 14: Nyquist plots of the two prepared samples with (a) x=0.025 and (b) x= 0.075
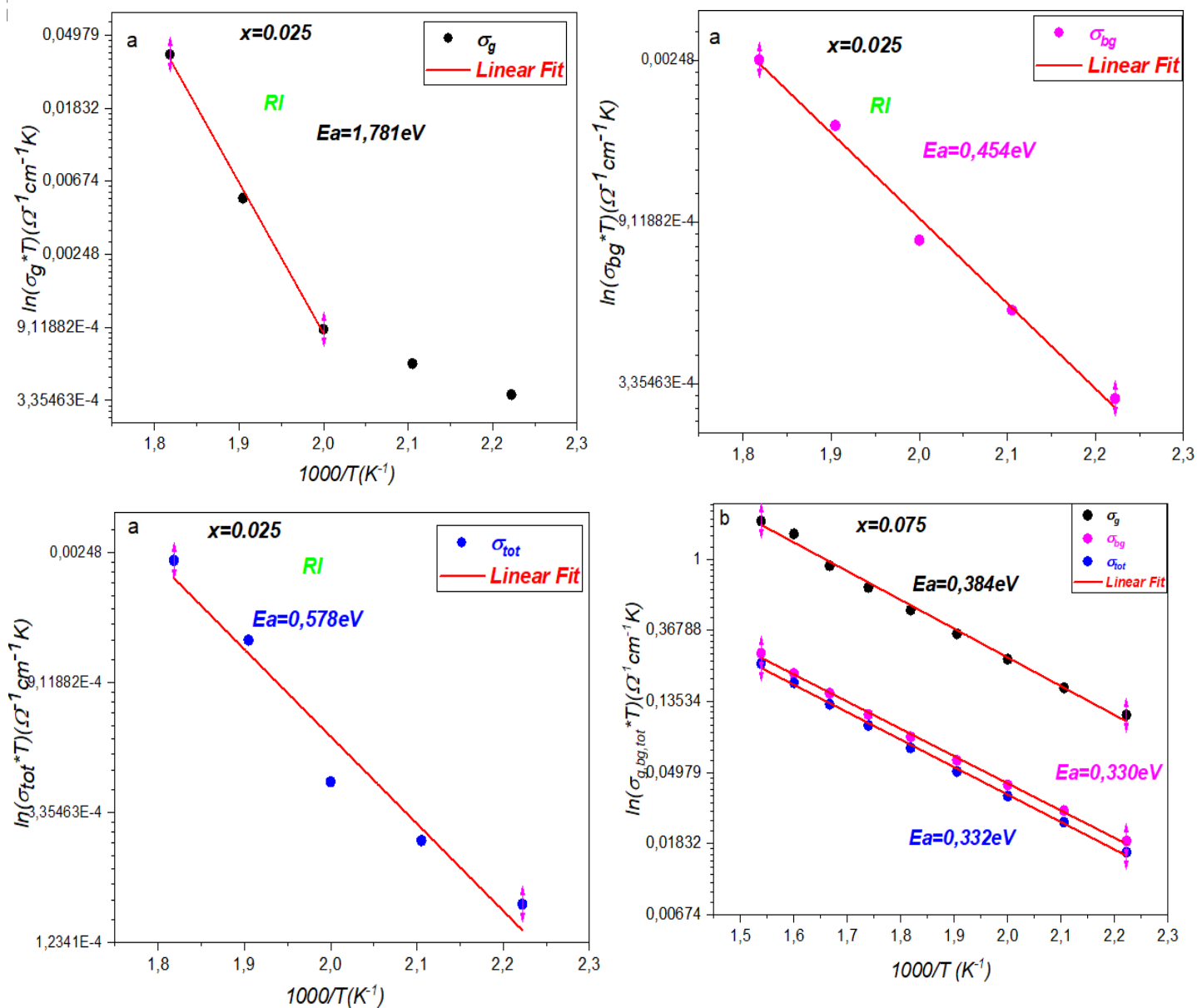
Figure 15: Variation of grain, grain boundary and total conductivities as function of 1000/T of Ba0.95Bi0.05Ti1-xFexO3 ((a) x=0.025 and (b) x= 0.075)
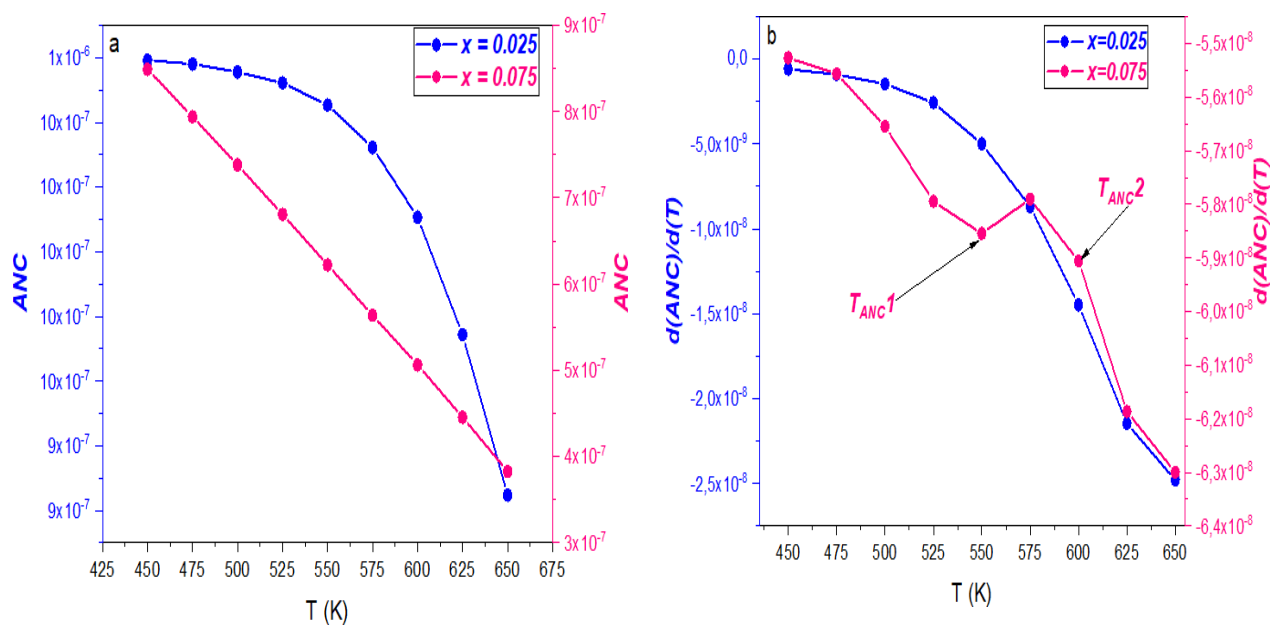
Figure 16: a) Temperature dependence of average normalized change (ANC) for Ba$_{0.95}$Bi$_{0.05}$Ti$_{1-x}$Fe$_x$O$_3$(x=0.025 and 0.075), b) Temperature dependence of the derivative of the average normalized change for both samples
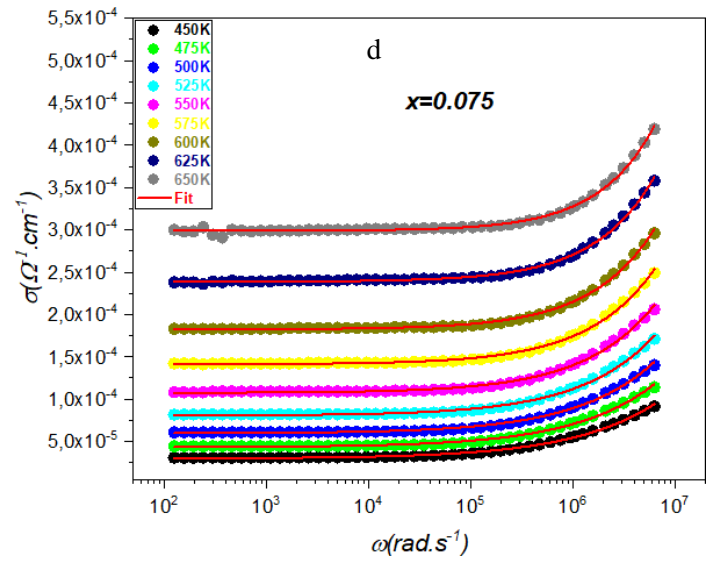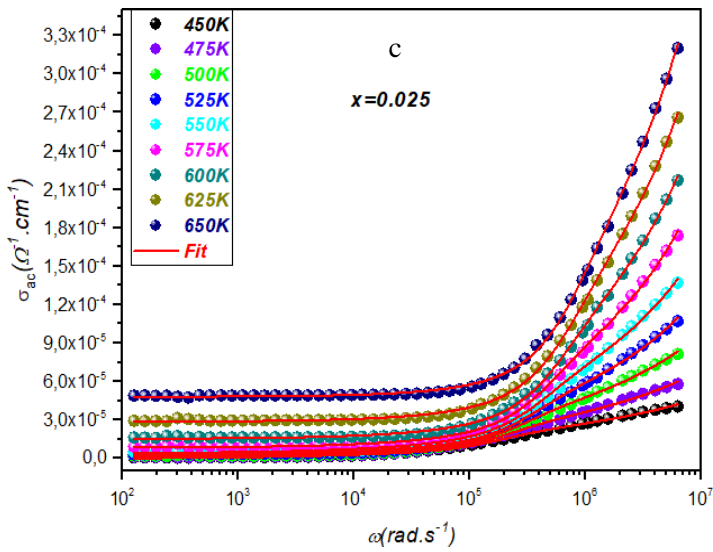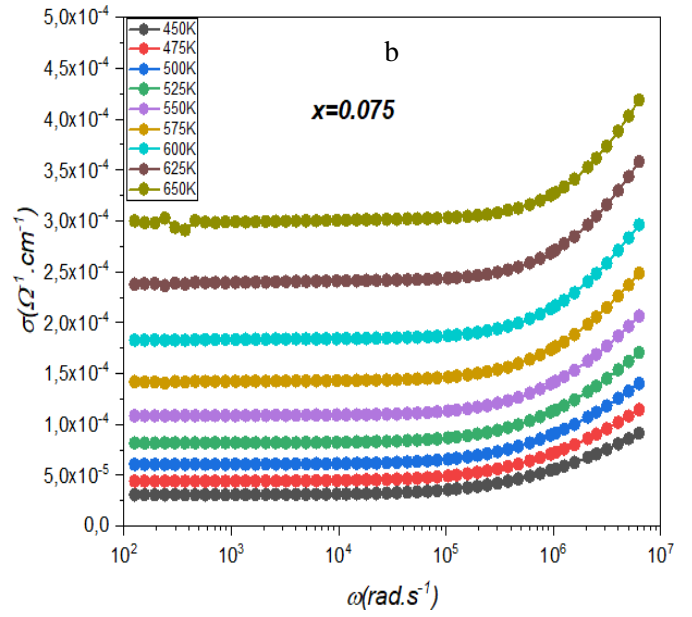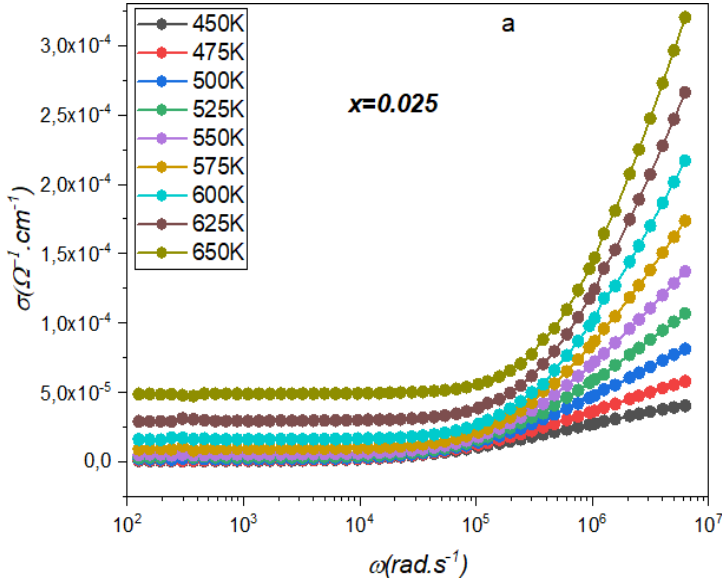
Figure 17: (a, b) Frequency dependence of the AC conductivity at different temperature for both samples with (a) x=0.025 and (b) x=0.075 //(c, d) fittingAC conductivity for both samples with (c) x=0.025 and (d) x=0.075
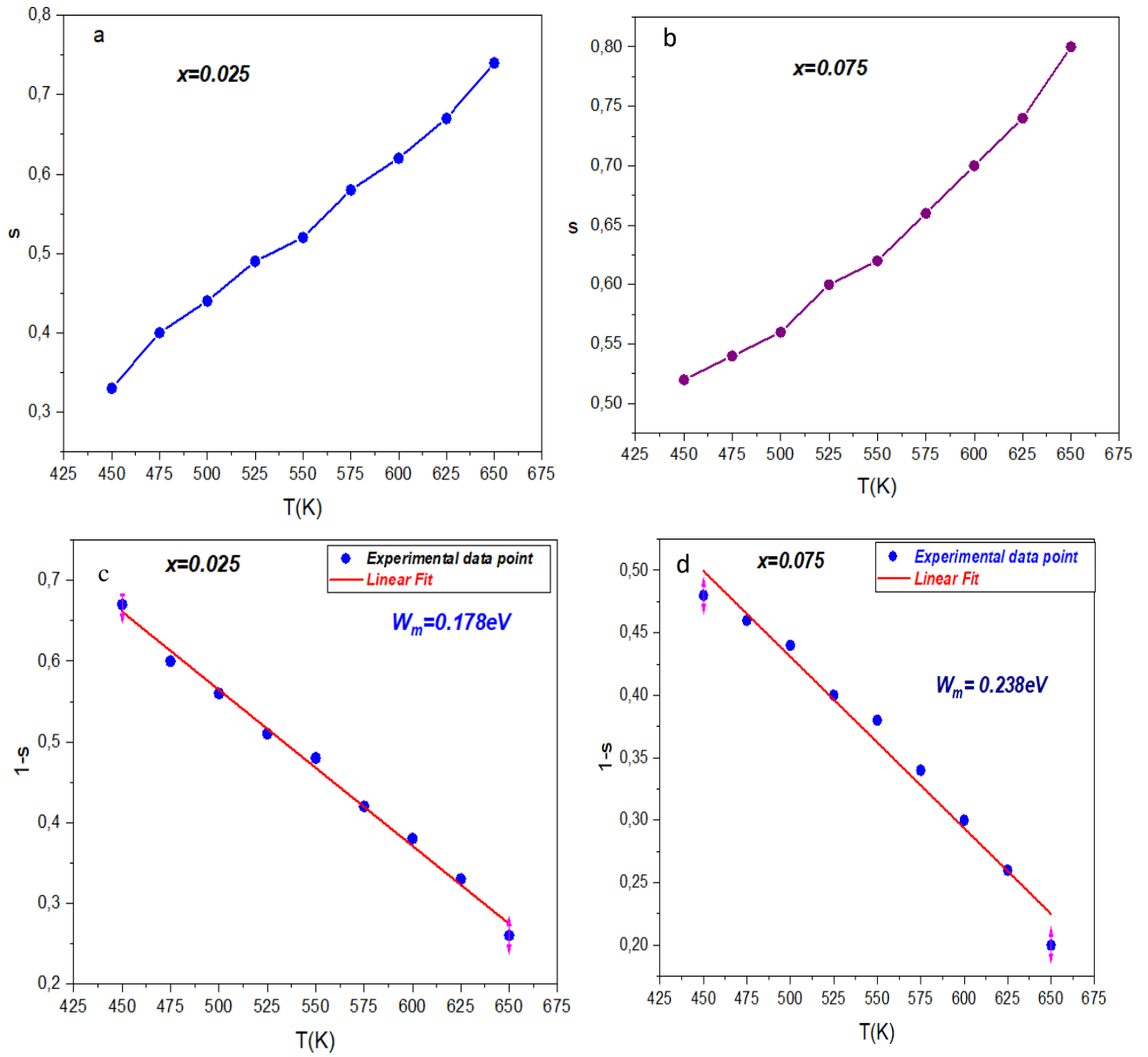
Figure 18 :(a, b) s-T variation of $Ba_{0.95}Bi_{0.05}Ti_{1-x}Fe_xO_3$ ((a) x=0.025 and (b) x= 0.075) and (c. d) Evolution of 1-s as function oftemperature for $Ba_{0.95}Bi_{0.05}Ti_{1-x}Fe_xO_3$ ((c) x=0.025 and (d) x=0.075)
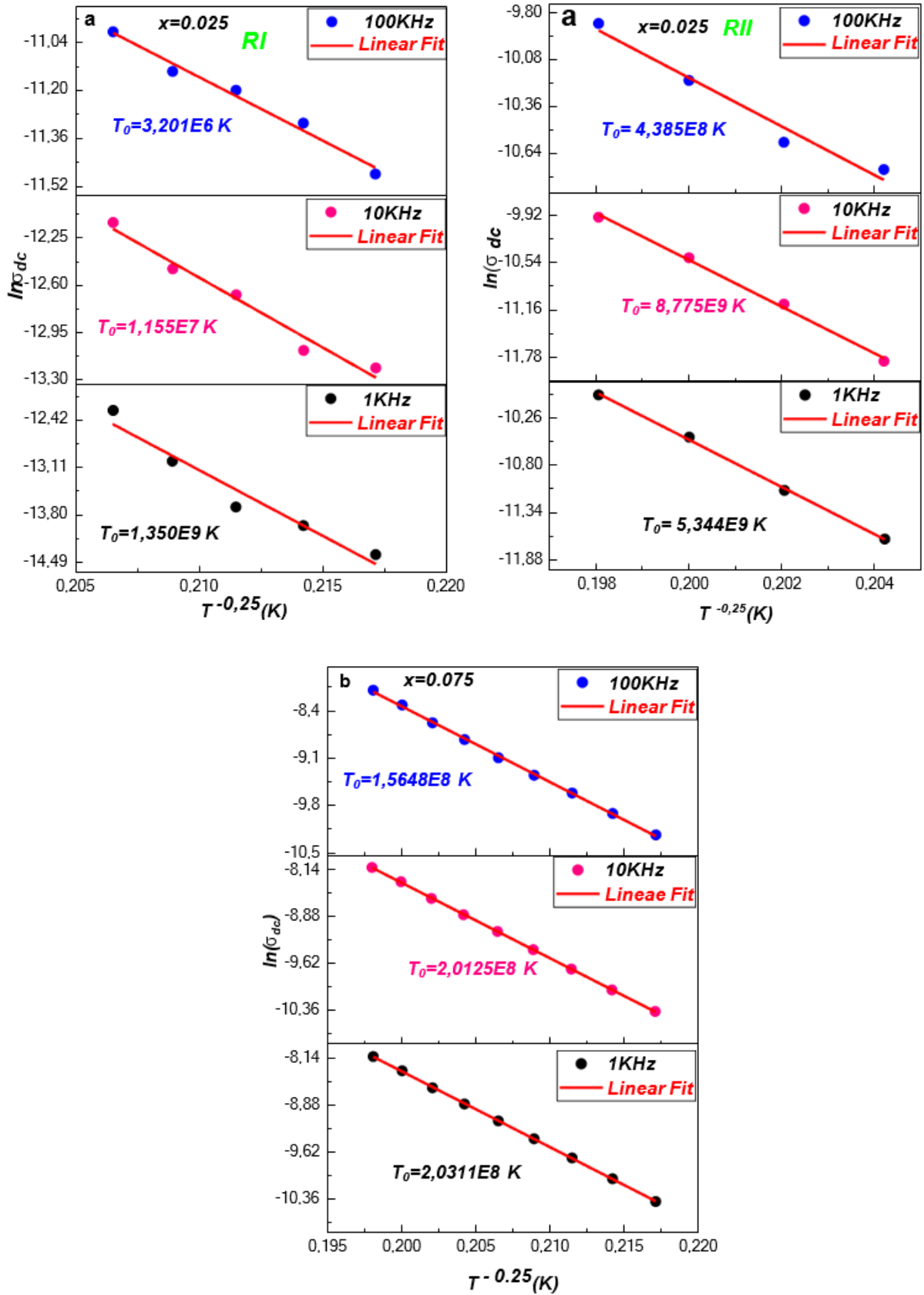
Figure 19: the variation of ln σ_DC versus T^{-0.25} (a/x=0.025 and b/x=0.075)
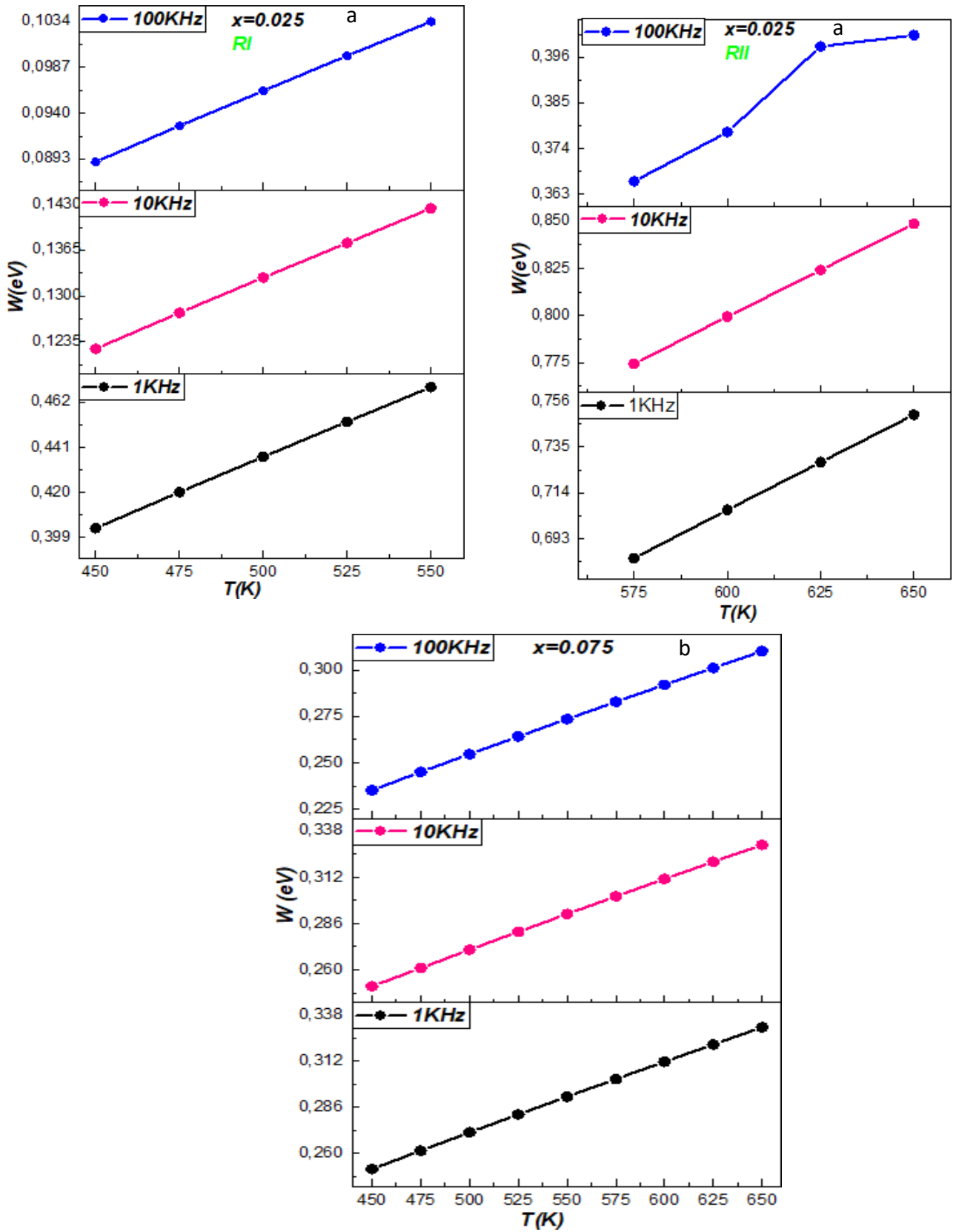
Figure 20: The variation of the hopping energy for Ba$_{0.95}$Bi$_{0.05}$Ti$_{1-x}$Fe$_x$O$_3$ ((a) x=0.025 and (b) x= 0.075)
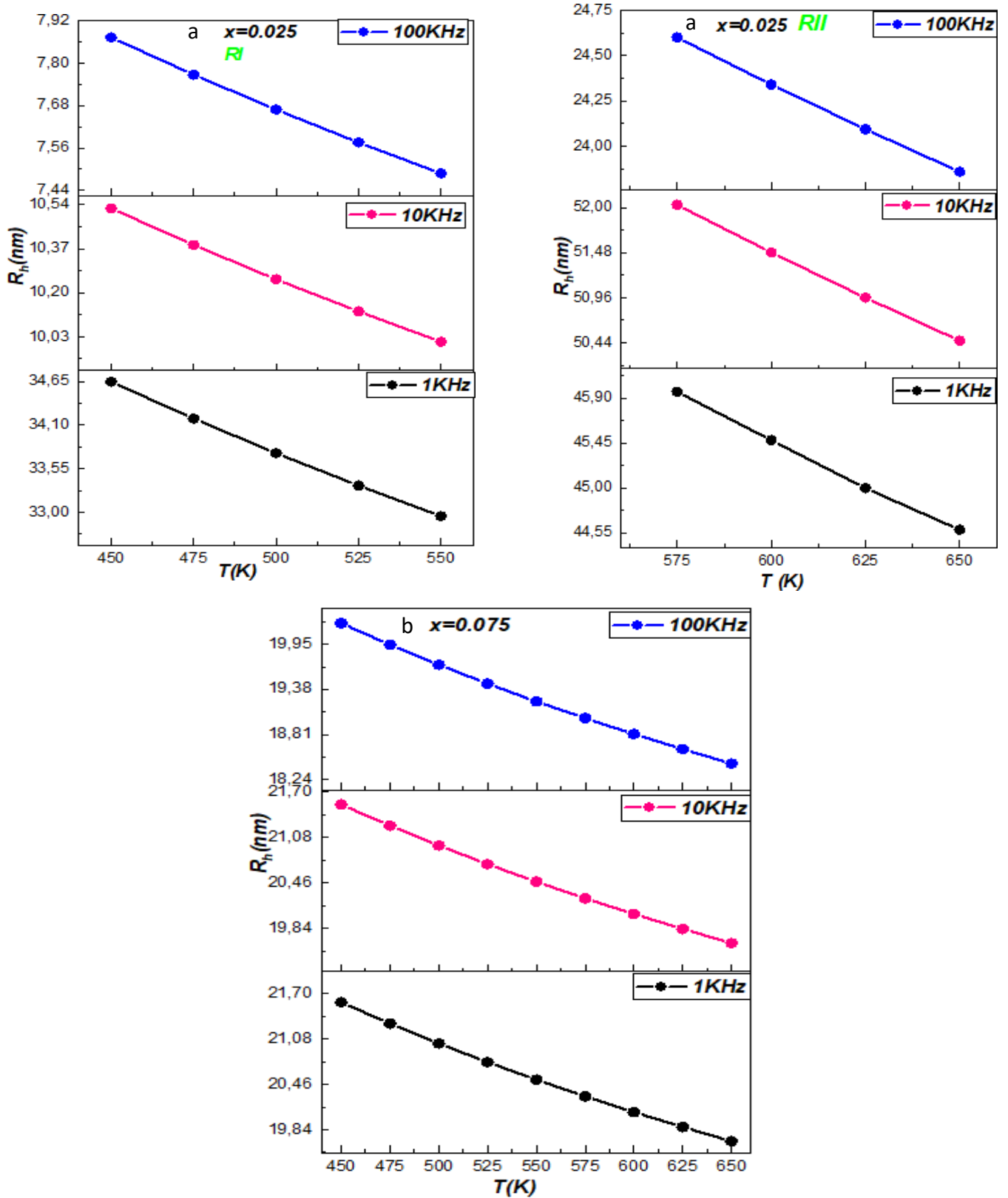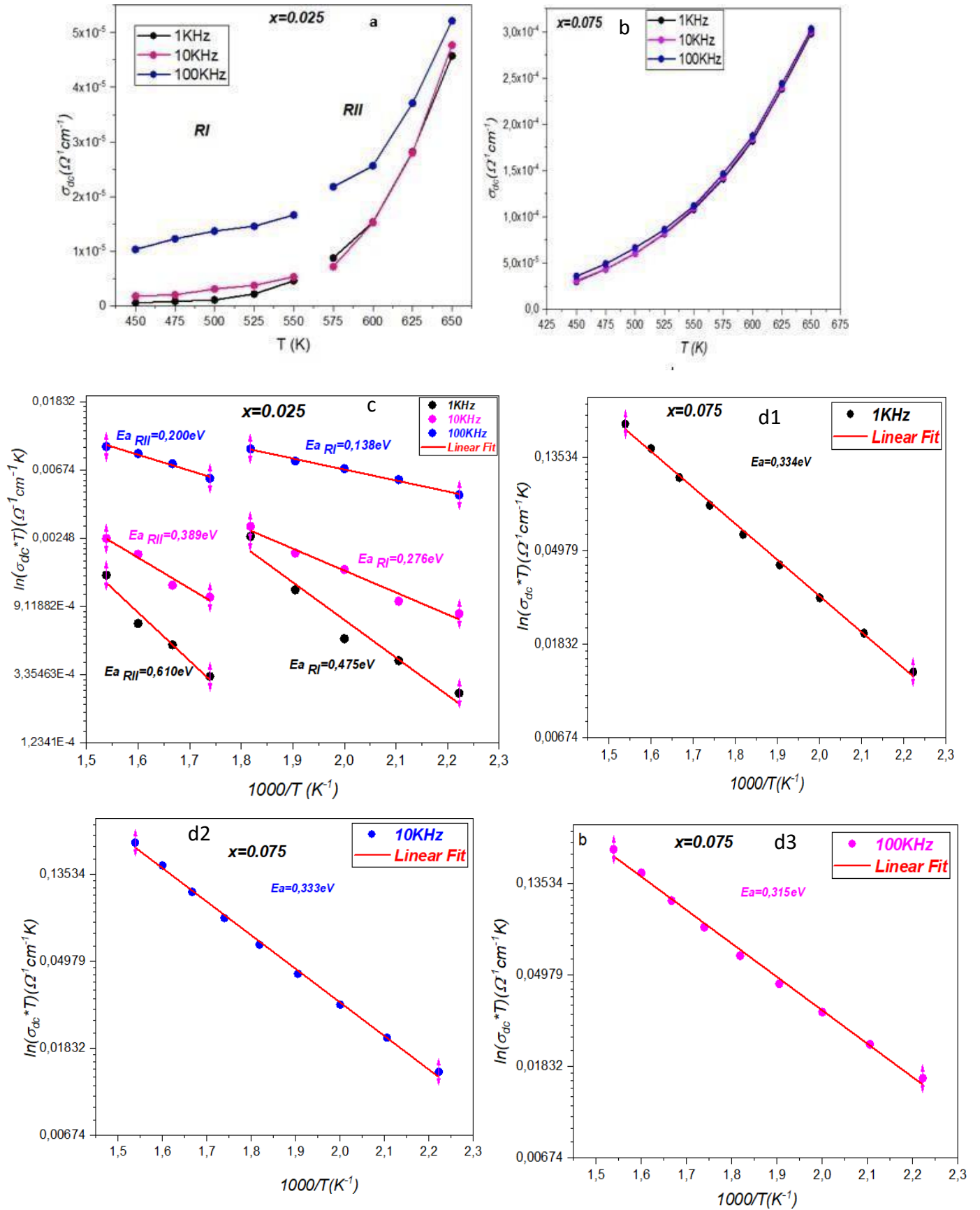
Figure 21: Thermal variation of hopping distance for Ba$_{0.95}$Bi$_{0.05}$Ti$_{1-x}$Fe$_x$O$_3$ ((a) x=0.025 and (b) x= 0.075)

Figure 22: (a, b) Thermal variation of AC conductivity at 1 KHz, 10 KHz and 100 KHz ((a) x=0.025 and (b) x= 0.075) and (c, d) Logarithmic variation of DC conductivity versus 1000/T for both samples ((c) x=0.025 and (d) x= 0.075)

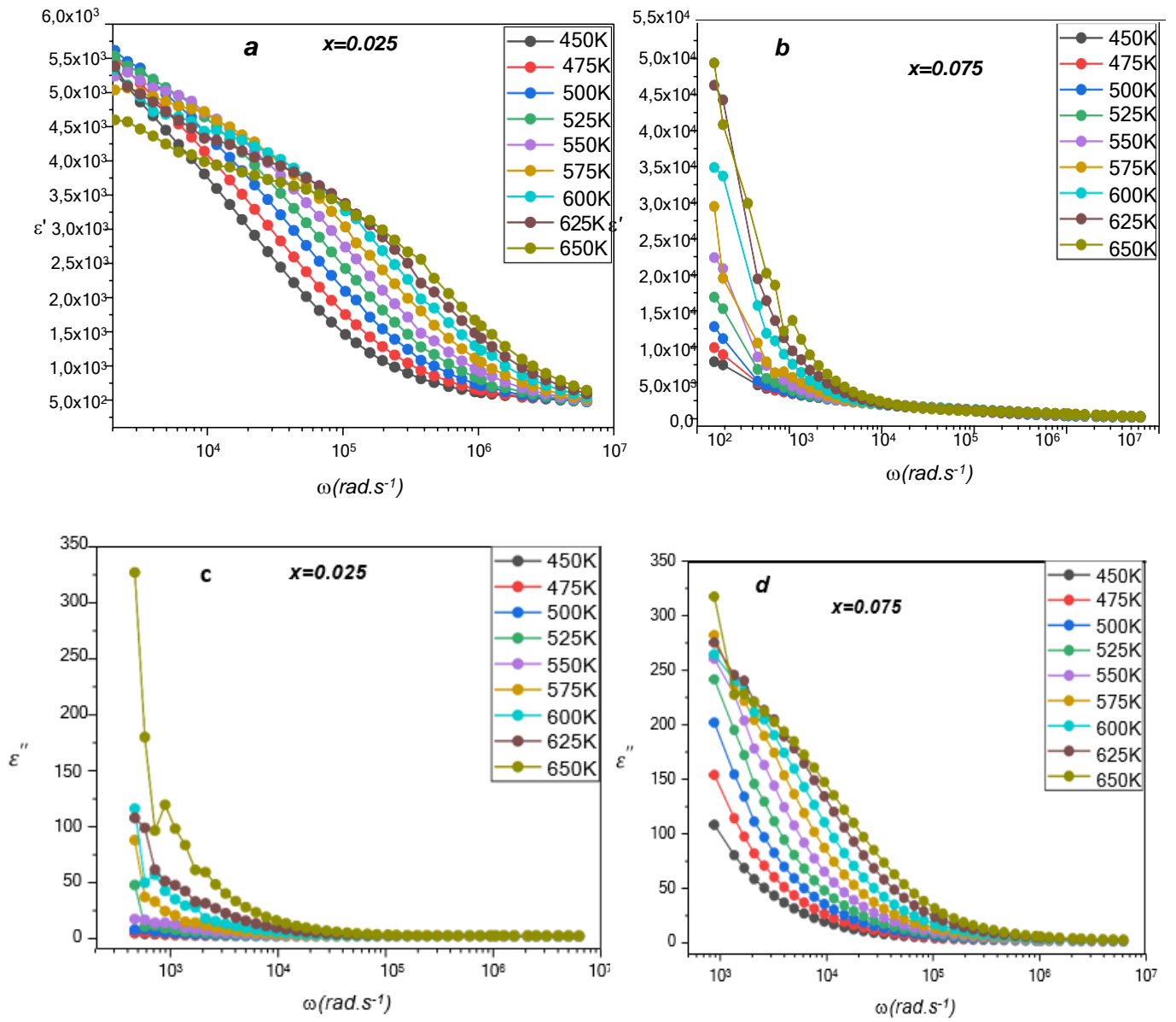*Figure 23: (a, b) Frequency dependence of the dielectric permittivity for $Ba_{0.95}Bi_{0.05}Ti_{1-x}Fe_xO_3$ ((a) x= 0.025 and (b) x= 0.075) and (c, d) Frequency dependence of the dielectric loss tan δ for $Ba_{0.95}Bi_{0.05}Ti_{1-x}Fe_xO_3$ ((c) x=0.025 and (d) x = 0.075)*

LIST OF TABLES

Table 5: Theoretical parameters obtained from the fitted data with the equivalent circuit for x=0.025

| | Grain contribution | | | | Boundary grain contribution | | | |
T(K)	$R_g(\Omega)$	C_g (E-11F)	CPE_g (F)	α_g	$Rb_g(\Omega)$	C_{bg} (E-11F)	CPE_{bg} (F)	α_{bg}
450	1.314e6	3.749	1.153E-6	0.239	1.564e6	13.05	1.533E-9	0.791
475	908250	8.471	1.106E-9	0.855	955280	3.397	1.138E-6	0.261
500	596970	2.609	1.260E-9	0.860	651870	3.419	2.160E-6	0.239
525	104280	2.854	8.887E-7	0310	336360	1.079	9.295E-10	0.904
550	15283	2.108	2.434E-8	0.561	234790	2.601	1.255E-9	0.857
575	57975	-------	5.760E-8	0.539	89407	-------	5.958E-10	0.989
600	9591		9.257E-9	0.663	72377		8.830E-10	0.909
625	8569		2.020E-8	0.617	36547		8.225E-10	0.926
650	6047		1.678E-8	0.632	21217		7.567E-10	0.934

Table 6: Theoretical parameters obtained from the fitted data with the equivalent circuit for x=0.075

| | Grain contribution | | Boundary grain contribution | | |
T(K)	$R_g(\Omega)$	C_g (E-9F)	$R_{bg}(\Omega)$	C_{bg} (E-8F)	α_{bg}
450	2562	0.062	15053	1.105	0.675
475	1846	2.828	10358	1.488	0.618
500	1300	2.784	7596	1.721	0.613
525	954.2	2.728	5654	1.842	0.613
550	717.1	2.681	4257	1.817	0.618
575	544.2	2.656	3249	1.692	0.626
600	419.1	2.637	2521	1.410	0.640
625	279.1	2.984	1968	1.259	0.651
650	242.9	2.626	1554	0.874	0.674

*Table 7: Activation energy obtained from the fitted data of ln ($\sigma_{g, bg, tot}$*T) as function as 1000/T*

Activation energy Ea(eV)

| | x=0.025 | | x=0.075 |
	RI	RII	
σ_g	1.781	0.956	0.384
σ_{bg}	0.454	0.692	0.330
σ_{tot}	0.578	0.782	0.332

Table 8: DC conductivity parameters

| | | x=0.025 | | x=0.075 |
		RI	RII	
$T_0(K)$	1KHz	1.350E9	5.344E9	2.031E8
	10KHz	1.155E7	8.775E9	2.012E8
	100KHz	3.201E6	4.385E8	1.564E8
$N(EF)(eV^{-1}cm^{-3})$	1KHz	1.257E16	3.178E15	3.063E15
	10KHz	1.475E18	1.934E15	8.433E16
	100KHz	5.303E18	3.870E16	1.084E17

*Table 9: Activation energy obtained from the fitted data of ln (σ_{ac}*T) as function as 1000/T*

Activation energy Ea(eV)

		1KHz	10KHz	100KHz
x=0.025	RI	0.475	0.276	0.138
	RII	0.610	0.389	0.200
x=0.075		0.334	0.333	0.315